Submitted for

National Plan for Science and Technology
King Saud University

Broadband Seismic Characterization of the Arabian Peninsula using 3-Component Seismic Array

Project No. : 08 - ENV516-2

Prof. Abdullah M. Al-Amri (PI)

Dr. Mohammed S. Fnais (CO - I)

October, 2011

Abstract

The Ar Rayn array project was initiated to provide observations of seismic waves in the Arabian peninsula and surrounding regions with a modern array of three-component instruments, the first of its kind in the Arabic-speaking world. The archive of observations obtained by this project ultimately will support improved models of crust and upper mantle structure in the Arabian peninsula, which in turn, will allow better monitoring of seismic events in the peninsula and shed light on broad structural features such as the volcanism of the western peninsula.

Seismic arrays suppress noise to provide better estimates of signal waveforms, and allow direct estimation of propagation parameters such as the slowness and azimuth of signals. Seismic monitoring with sparse networks of stations traditionally has relied on arrays to improve detection and location performance, especially to reduce magnitude thresholds by boosting signal to noise ratios over those observed with single stations. Noise suppression performance of an array depends on the array geometry, especially the array aperture and sensor separation.

The Ar Rayn array was a small-aperture, high-frequency regional array deployed in the Arabian shield near its eastern edge. It consisted of a central broadband three-component sensor (STS-2) and eight short-period three-component sensors spread across a 3.5 kilometer aperture. Data were recorded continuously at 100 samples per second on Quanterra Q330 data loggers at individual sensors of the array. The data were archived and processed at KSU, where basic quality control, format conversion and event extraction functions were performed.

Before this deployment, no regional seismic arrays existed in the Arabian Peninsula. Beyond its value to provide constraints on geophysical structure, the array is a teaching tool providing new opportunities for faculty and students to explore and learn wave propagation effects and array signal processing. The project also provides opportunities for research on new data processing techniques including combinations of polarization filtering and beamforming and adaptive array processing.

We used data from the array to improve our understanding of regional and teleseismic arrivals in the context of crustal and upper mantle structure inferred from previous studies. Ground truth for seismic arrivals was obtained from

catalogues provided by the Saudi Geologic Survey (SGS), the King Abdulaziz City for Science and Technology (KACST) and international organizations (USGS, IDC). We applied traditional array signal processing techniques, such as slowness and azimuth estimation to document how seismic structure biases these measurements away from radially stratified earth models.

Our preliminary noise study showed that the site is exceptionally quiet with noise levels near the USGS low noise model for frequencies in the central band from 50 seconds to 5 Hz. This behavior is consistent with the nearby GSN station RAYN. At lower frequencies, the horizontal components showed high noise levels, possibly due to instrumental characteristics. The array appears to be among the best sites in the world for ground noise levels and detection. The m_b detection threshold for the distance range of 5 -10 degrees is about m_b = 2.7-3.0 assuming the signal-to-noise ratio of 3 dB or better.

Analyses of teleseismic P phase coherence and polarization across the array aperture demonstrate uniformity of installation and instrumentation, essential characteristics for proper array operation. Beamforming results demonstrate that the array will improve estimates of P arrival times and waveforms for small events in the region. Since the array is one of only a few with three-component stations deployed at all elements, it should provide opportunities to examine more sophisticated combinations of beamforming and polarization filtering, and phase identification and association through three-component FK analysis. Results from local and regional events confirm this expectation.

Acknowledgments

The authors would like to express their thanks and gratitude to the National Plan for Science, technology and innovation at KACST for funding this project (**Grant no. 08-ENV516-2**). We extend our sincerest thanks to Mr. Mostafa Hemida, Fahad Al-Omairah and Ahmad Rabea for their supervising construction and seismic data collection.

Table of Contents

List of Figures

1. Introduction

Good introductions to array signal processing are available from, for example, the New Manual of Seismological Observatory Practice [2009]. Much of the material in the following section follows that introduction. A good textbook introduction is available in Array Signal Processing: Concepts and Techniques [Johnson and Dudgeon, 1993]. For introductions, see also Rost and Thomas [2002] and Douglas [2003]. For advanced techniques, see Van Trees [2002].

1.1 Array Signal Processing

Seismic arrays differ from networks of seismic stations principally in the techniques used for data analysis. The principal array assumption is that waves incident on the array have planar structure (i.e. the wavefronts are linear, perpendicular to the direction of propagation, see Figure 1). This assumption, in turn requires that the incident signals be identical apart from propagation delays. Consequently, most array processing methods require high signal coherence across the array aperture. This requirement places constraints on array geometry, principally the size of the aperture, but also requirements for uniform sensor emplacement (i.e. consistent bedrock contact) across the aperture. Because estimates of direction and velocity of seismic arrays require measurement of small propagation time differences among sensors across the aperture, array analysis requires stable, high precision relative timing among all stations.

Array signal detection capability superior to that of individual stations is obtained by beamforming operations, which combine the outputs of multiple seismometers in a manner to enhance signals and suppress noise so as to increase the signal-to-noise ratio (SNR) of the observation. Arrays also provide estimates of station-to-event azimuth (backazimuth) and of the apparent (horizontal) velocity of seismic waves that sweep across the aperture. These estimates are important to phase association (event building) and phase identification, important steps in event location.

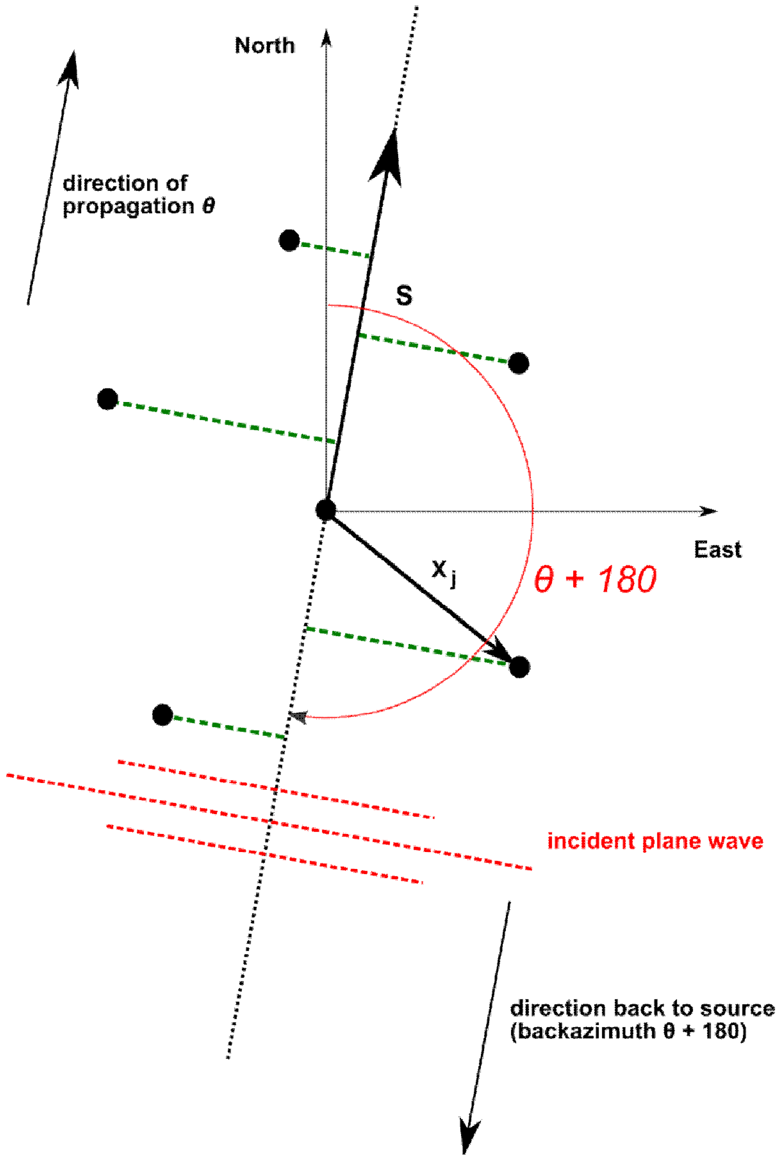

Figure 1 Definition of array quantities: slowness vector s, station location vector **x**$_i$, and azimuth ☐ of propagation.

An array is a collection of seismometers with locations specified as vectors $\mathbf{x}_i$ (here bold fonts indicates vector quantities) referenced to a common point. That point may be a central station of the array or an arbitrary geographic location (often taken as the centroid of the element locations). Figure 1 shows geometric definitions of array element locations and propagation characteristics of plane waves all projected onto the surface of the earth. Here we have defined the direction of wave travel with respect to north (positive clockwise through east) by the angle θ and the backazimuth (direction from the array back to the source) as $\theta + 180$ degrees. The slowness vector:

$$\mathbf{s} = \begin{bmatrix} s_{north} \\ s_{east} \end{bmatrix} = \frac{\sin i}{v} \begin{bmatrix} \cos\theta \\ \sin\theta \end{bmatrix} \tag{1}$$

describes the direction and speed of travel of the incident wave. Here, v is the medium velocity near the surface at the array location, and i is the angle of incidence that the wave (which is traveling in the 3-dimensional medium) makes with the vertical axis (see Figure x). The quantity $\sin i/v$ is known as the ray parameter and represents the speed of propagation of the wavefield restricted to the surface of the earth. The reciprocal of the ray parameter is called the apparent velocity of the wave.

Under the plane wave model, the signal observed by a single sensor of the array has the form:

$$r_j(t) = f(t - \Delta_j) + n_j(t) \tag{2}$$

which makes explicit the expectation of a common signal across the array apart from propagation delays Δ_j and noise, which, in reality often is correlated among sensors, but in most algorithms is considered to be uncorrelated. The variable j indexes elements of the array as shown in Figure 1. The delays are computed as simple projections of the sensor location vectors onto the slowness vector (Figure 1):

$$\Delta_j = \mathbf{s} \cdot \mathbf{x}_j \tag{3}$$

Under the plane wave model, seismic arrays improve SNR with beamforming, which shifts the observed waveforms to align signals propagating from an event of interest, then sums the resulting waveforms. If the signals are perfectly correlated across the array aperture, they sum constructively. If the noise is uncorrelated among sensors, it sums destructively. The result is an increase in the power SNR by a factor of N where N is the number of sensors in the array (equivalently an increase in the amplitude SNR by a factor of $\sqrt{N}$). Beamforming is described by the equation:

$$b(t) \;=\; \frac{1}{N}\sum_{j=1}^{N} r_j\left(t+\Delta_j\right) \tag{4}$$

Parameter estimation tasks, such as estimation of wave direction and apparent velocity are usually performed with a technique known as frequency-wavenumber (FK) spectral analysis. This method decomposes the incident wavefield into narrowband frequency components and represents the signal as a superposition of complex exponential plane waves. If we collect the waveforms observed across the array into a vector:

$$\mathbf{r}(t) \;=\; \begin{bmatrix} r_1(t) \\ r_2(t) \\ \vdots \\ r_N(t) \end{bmatrix} \tag{5}$$

A narrowband signal can be approximated as the real part of a complex analytic expression:

$$r_j(t) \;\sim\; \boldsymbol{Re}\left\{\rho_j(t)\, e^{i\omega t}\right\} \tag{6}$$

The complex amplitude $\rho_j(t)$ is a slowly-varying in time. The radial frequency is denoted by $\omega = 2\pi f$ and represents the center frequency of the narrow band. Here $i = \sqrt{-1}$ and $\mathbf{s}_o$ is the slowness vector of the incident plane wave. The vector signal representation for the array is, similarly:

$$\mathbf{r}(t) \;=\; \boldsymbol{Re}\left\{\begin{bmatrix} \rho_1(t) \\ \rho_2(t) \\ \vdots \\ \rho_N(t) \end{bmatrix} e^{i\omega t}\right\} \tag{7}$$

With reference to equations (3) and (4), the beam can be written as:

$$b(t) \;=\; \boldsymbol{Re}\left\{\frac{1}{N}\, e^{i\omega t}\sum_{j=1}^{N} e^{i\omega(\mathbf{s}\cdot\mathbf{x}_j)}\rho_j\left(t+\Delta_j\right)\right\} \tag{8}$$

By defining the wavenumber vector

$$\mathbf{k} \;=\; \omega\mathbf{s} \tag{9}$$

and using the fact that the complex envelopes are slowly varying ($\rho_j(t+\Delta_j) \approx \rho_j(t)$, the narrowband beam can be approximated by:

$$\begin{aligned} b(t) &= \boldsymbol{Re}\left\{\frac{1}{N}\, e^{i\omega t} \sum_{i=1}^{N} e^{i\mathbf{k}\cdot\mathbf{x}_j}\, \rho_j(t)\right\} \\ &= \boldsymbol{Re}\left\{\frac{1}{N}\, e^{i\omega t}\left[e^{i\mathbf{k}\cdot\mathbf{x}_1} \quad e^{i\mathbf{k}\cdot\mathbf{x}_2} \quad \cdots \quad e^{i\mathbf{k}\cdot\mathbf{x}_N}\right]\begin{bmatrix}\rho_1(t)\\ \rho_2(t)\\ \vdots \\ \rho_N(t)\end{bmatrix}\right\} \end{aligned} \tag{10}$$

The FK spectrum is a map of the average power in the beam as a function of assumed wavenumber $\mathbf{k}$ (or equivalently slowness $\mathbf{s}$):

$$P(\omega, \mathbf{k}) \;=\; \frac{1}{T}\int_0^T |b(t)|^2\, dt \tag{11}$$

where T is the length of an integration interval encompassing a seismic arrival of interest. With some manipulation, equation (11) can be written compactly in terms of the so-called steering vector (which appears in equation (10)):

$$\boldsymbol{\varepsilon}(\mathbf{k}) \;=\; \begin{bmatrix} e^{i\mathbf{k}\cdot\mathbf{x}_1} \\ e^{i\mathbf{k}\cdot\mathbf{x}_2} \\ \vdots \\ e^{i\mathbf{k}\cdot\mathbf{x}_N}\end{bmatrix} \tag{12}$$

and the covariance matrix for the observed vector signal:

$$\mathbf{R}(\omega) \;=\; \frac{1}{T}\int_0^T \begin{bmatrix}\rho_1(t)\\ \rho_2(t)\\ \vdots \\ \rho_N(t)\end{bmatrix}\left[\rho_1^*(t) \quad \rho_2^*(t) \quad \cdots \quad \rho_N^*(t)\right] dt \tag{13}$$

With these definitions:

$$P(\omega, \mathbf{k}) \;=\; \boldsymbol{\varepsilon}^H(\mathbf{k})\mathbf{R}(\omega)\boldsymbol{\varepsilon}(\mathbf{k}) \tag{14}$$

In these expressions, the superscript * denotes the conjugation operation for a scalar and the superscript H denotes the conjugate transpose operation for a vector. Figure 2 provides an interpretation of the spectrum in a simple case involving two incident plane waves traveling at slightly different speeds. Interpreted properly, the FK spectrum shows peaks in the direction of the sources from the array. The distance of the peak from the origin is inversely proportional to the apparent (horizontal) velocity of the waves.

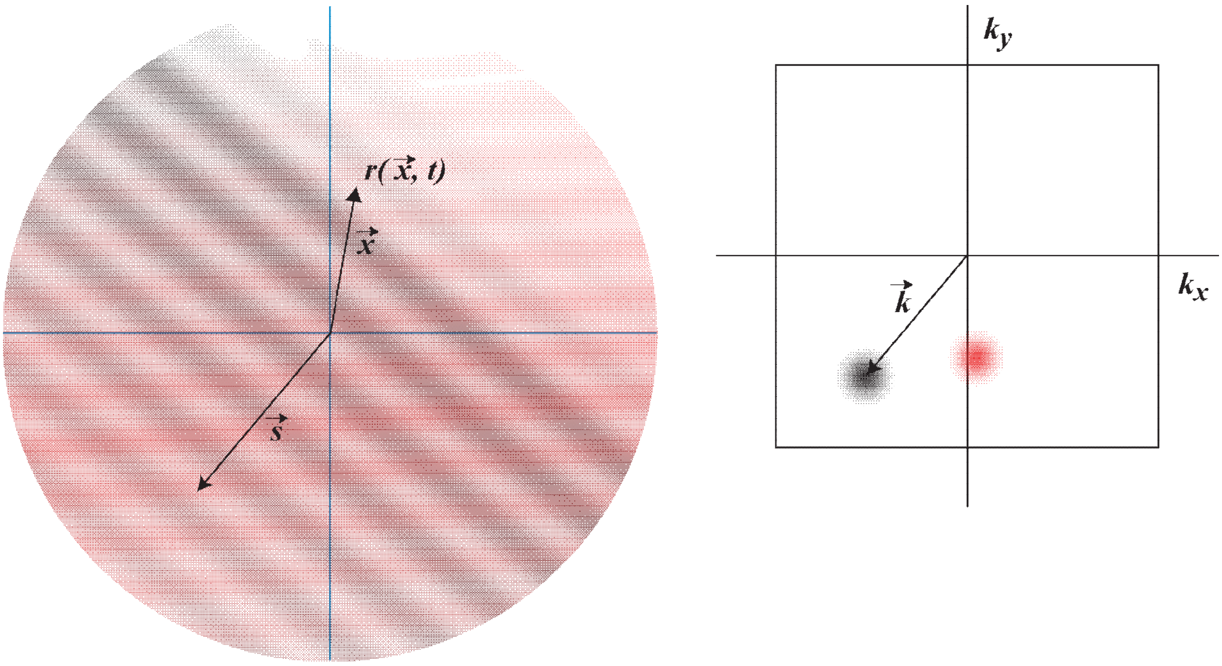

Figure 2 Cartoon depicting the interpretation of an FK spectrum. At left the wavefield incident on an aperture is shown to consist of two superimposed narrowband plane waves, one (black) arriving from the southeast and a second (red) faster wave arriving from the south. The slowness vector **s** has been plotted backwards in this figure to emphasize the direction to the source. At right is a depiction of the FK spectrum, which has non-zero values in the third quadrant (southeast) corresponding to the first wave and to the south corresponding to the second wave. The wavenumber spectrum is plotted with wavenumbers reversed in sign to allow interpretation of the spectrum in terms of backazimuth to the source.

In the early days of seismic array signal processing, algorithms were developed to suppress undesired signals and noise with exploitable propagating structure (plane waves). These methods are commonly referred to as adaptive beamforming algorithms. The technique commonly attributed to Capon et al. [1967] uses a set of filters operating on the (shifted) outputs of the array elements to minimize the power of the beam subject to a constraint that a signal propagating from the desired direction at the desired velocity be passed without distortion. Mathematically, this operation is described by the following:

$$b(t) = \sum_{j=1}^{N} \left(h_j \otimes \tilde{r}_j\right)(t) \qquad \tilde{r}_j(t) = r_j\left(t + \Delta_j\right)$$
$$\min_{\{h_j\}} \int_0^T |b(t)|^2 \, dt \qquad s.t. \sum_{j=1}^{N} h_j(t) = \delta(t) \tag{15}$$

The symbol ⊗ refers to convolution between the impulse responses $h_j(t)$ and the corresponding shifted sensor signals $\tilde{r}_j(t)$ (delayed to align the desired signals across the array according to the plane wave model). The filters are chosen to minimize the power of the beam, subject to the constraint that their impulse responses sum to a Dirac delta function. This condition assures that signals propagating according to the plane wave model from the desired direction and velocity pass through to the beam without distortion. This algorithm can be effective in suppressing unwanted signals more than standard beamforming (equation 4). We give an example later in the report which uses an efficient conjugate gradient method [Kobayashi, 1970] for determining the filter impulse responses.

1.2 Three Component Processing

Figure 3 illustrates the types of polarization supported by elastic waves. There are three types of linear polarization and two types of elliptical polarization (only one is indicated). In theory, body waves are linearly polarized, which means that the motion of the ground during passage of the wave is in a straight line. For compressional (P) waves, this motion is in the direction of travel of the waves and for shear (S) waves it is orthogonal to the direction of travel. Shear wave polarization is of two types: shear vertical (SV), in which the motion of a particle in the ground is confined to a vertical plane defined by the direction of travel and shear horizontal (SH), in which the particle motion is parallel to the ground surface. Surface waves exhibit two types of polarization: Love waves have SH type polarization and Rayleigh waves exhibit elliptical polarization. In elliptically polarized waves, particle motion describes an ellipse which may be either retrograde (counterclockwise as indicated in the figure) or prograde (clockwise). As a practical matter, only low-frequency waves and the initial arrivals of body waves have discernable polarization as described here. Elsewhere, scattering tends to obscure ideal particle motion. Often the particle motions of initial P waves and low-frequency surface waves are most readily observed. Figure 4 illustrates that compressional wave linear particle motion is described by a particle motion vector:

$$\boldsymbol{\gamma} = \begin{bmatrix} \cos i \\ \sin i \cos \theta \\ \sin i \sin \theta \end{bmatrix} \tag{16}$$

parameterized by the azimuth θ of wave propagation (angle from north through east) and i is the incidence angle that the wave direction makes with the vertical axis. A perfectly polarized P wave has a three-component particle motion $\mathbf{p}(t)$ described by a time history $f(t)$ and the polarization vector:

$$\mathbf{p}(t) = \boldsymbol{\gamma}\, f(t) \tag{17}$$

The polarization vector may be estimated through principal components analysis of a sample covariance matrix calculated from the recorded signal:

$$\mathbf{r}(t) = \mathbf{p}(t) + \mathbf{n}(t) \tag{18}$$

Here $\mathbf{n}(t)$ is ambient noise. The covariance matrix $\mathbf{C}$ is estimated from sampled data:

$$\mathbf{C} = \sum_n \mathbf{r}(n\Delta t)\, \mathbf{r}^T(n\Delta t) \tag{19}$$

where the superscript T indicates the transpose operation. If the noise is small compared to the signal, the estimated particle motion vector $\hat{\boldsymbol{\gamma}}$ is obtained as the principal eigenvector of $\mathbf{C}$. The corresponding eigenvalue is the energy of the signal:

$$E = \sum_n f^2(n\Delta t) \tag{20}$$

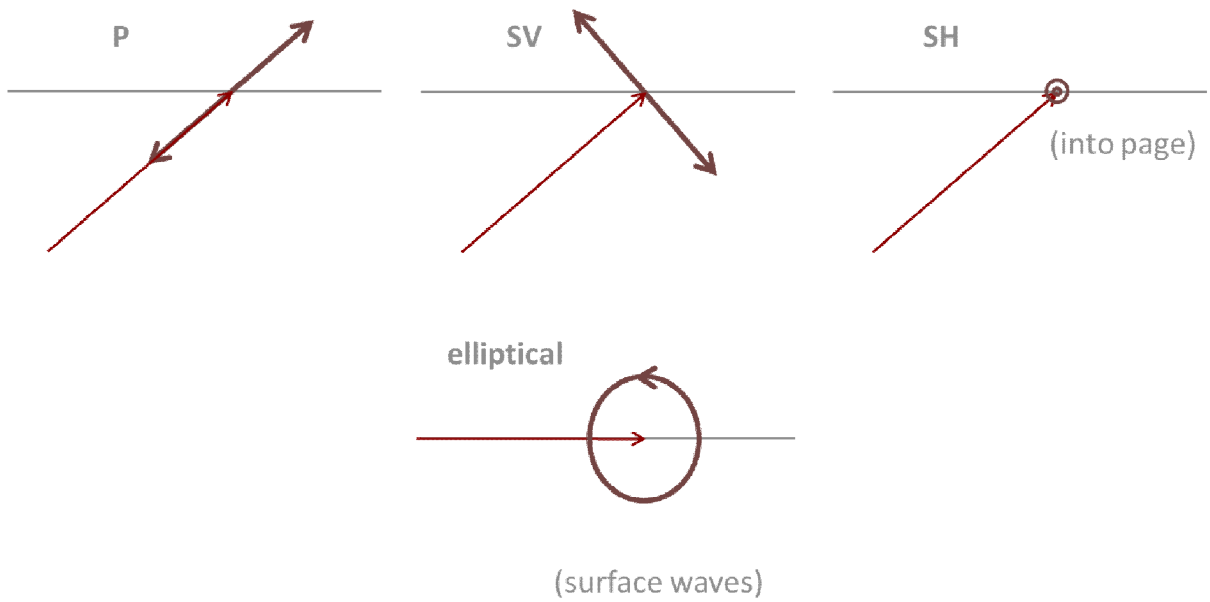

Figure 3 Types of polarization of seismic waves. Polarization refers to the motion that a particle in the ground undergoes during the passage of a seismic wave.

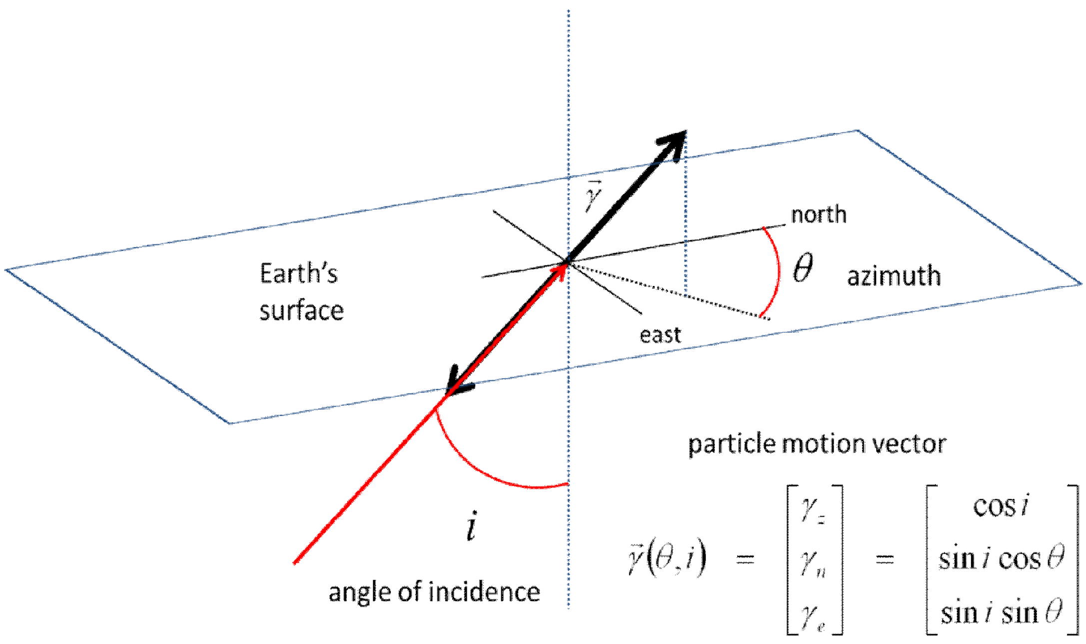

Figure 4 Definition of terms for particle motion linearly polarized in the direction of wave travel. This is the type of polarization exhibited by compressional (P) waves.

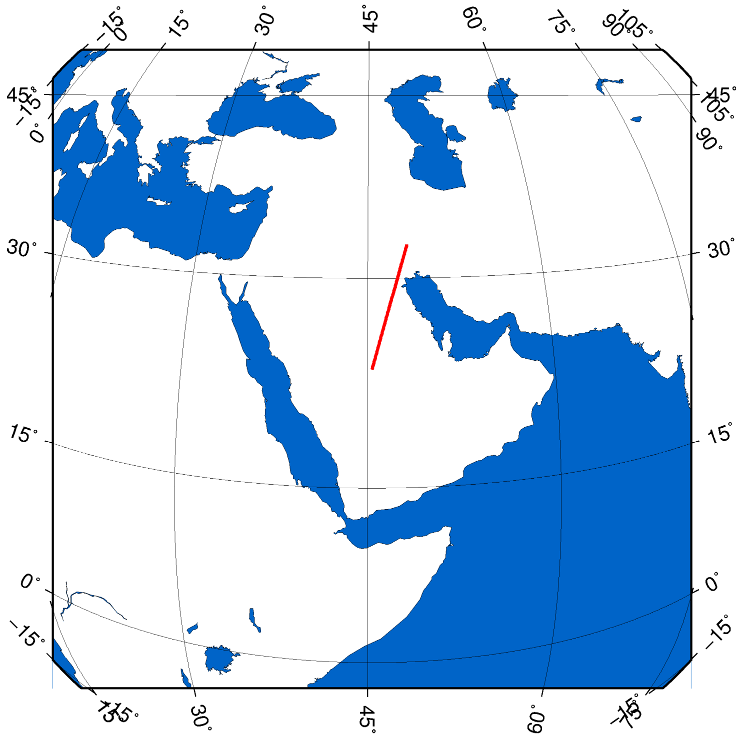

Figure 5 Location of magnitude 5.0 event used to illustrate linear particle motion. This event is about 1036 kilometers to the north northwest of the Ar Rayn array.

An example of P particle motion is illustrated with the event of Figure 5. This is a (NEIC) magnitude 5.0 earthquake about 1036 kilometers from the array. The vertical component waveforms from the stations that were recording at the time are shown in Figure 6. The top trace shows the data from the broadband vertical station at the center of the array. The signals have lower frequency content than those from the other stations, particularly the pronounced Rayleigh wave at the end of the record. The four regional phases (in order, left to right) Pn, Pg, Sn and Lg are well-recorded for this event. The Pg and Lg phases arrive late in this record compared to other parts of the world due to the deep sediments that they travel through in the Arabian Gulf along the path to the station. Figure 7 shows an enlargement of the initial Pn phase at station AR11 and Figure 8 displays plots of the particle motion for this phase window in the horizontal plane (left) and in the vertical plane restricted to the strike of particle motion. The linearity of the motion is striking in this example. This figure shows a strong resemblance to the sketch of Figure 4.

Projections of the polarization vector obtained by principal component analysis as described above onto these two planes are shown in red in Figure 8. The estimated back azimuth is 15.6 degrees, which is remarkably close to the true back azimuth of 15.7 degrees. This is chance agreement, as will be seen in the later examples.

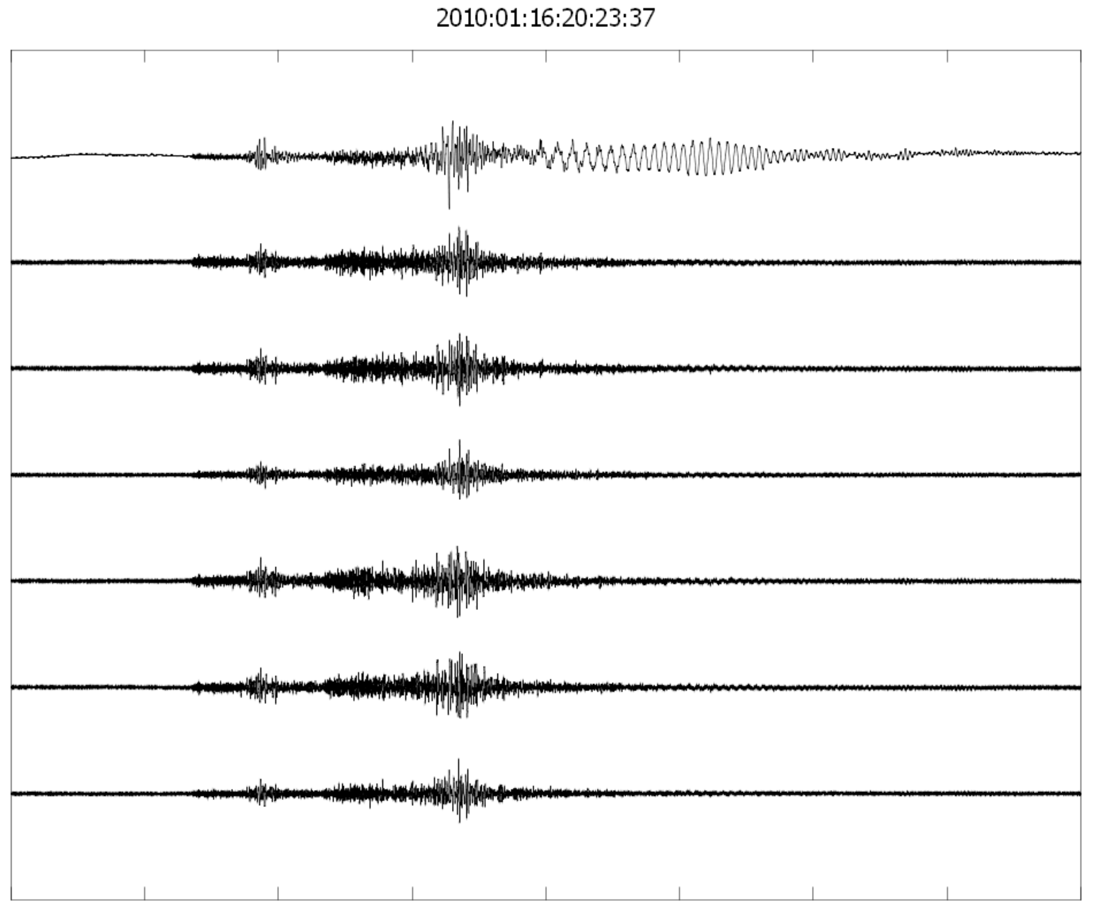

Figure 6 Ground motion recorded by the vertical-component seismographs of the Ar Rayn array for the magnitude 5 event. The top trace is from the broadband station at the center of the array. Note the surface (Rayleigh) wave well-dispersed by the deep sediments of the Arabian Gulf. The other six traces are from the short-period stations that were operating at the time. These show (in order of arrival) Pn, Pg, Sn and Lg phases. The Pg and Lg phases are slower in this region than in other parts of the world due to propagation through the deep sediments of the eastern Arabian peninsula.

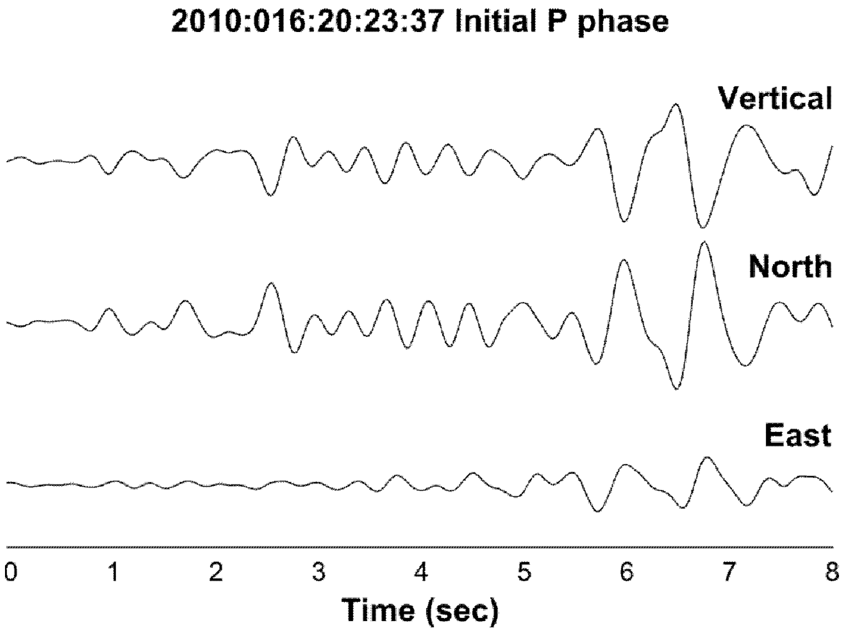

Figure 7 Three-component motion at station AR11 for the initial P arrival. Note the almost perfect mirror-image symmetry of the vertical and north channels. This event is close to due north of the array.

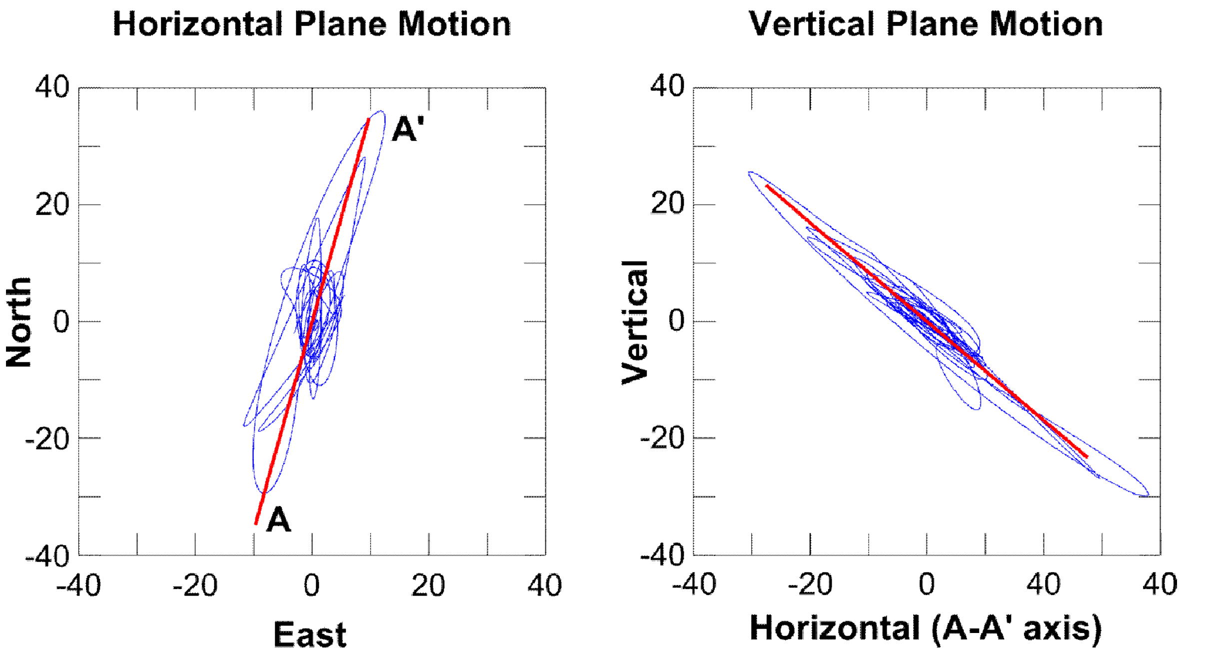

Figure 8 Plots of motion in the horizontal plane (left) and the vertical plane (right) show this initial P phase to be highly polarized. The red lines indicate the axis of linear motion best fitting the particle motion, determined from principal components analysis.

1.3 Combining Polarization Processing and Beamforming

An array of three component stations is capable of measuring the polarized wavefield across a spatial aperture. Provided the aperture is small compared to the range to the event, a plane wave model for the signal is a good approximation:

$$\mathbf{r}(t) = \begin{bmatrix} \boldsymbol{\gamma}\, f(t-\Delta_1) \\ \boldsymbol{\gamma}\, f(t-\Delta_2) \\ \vdots \\ \boldsymbol{\gamma}\, f(t-\Delta_N) \end{bmatrix} = \begin{bmatrix} \mathbf{r}_1(t) \\ \mathbf{r}_2(t) \\ \vdots \\ \mathbf{r}_N(t) \end{bmatrix} \tag{21}$$

The signal is a vector with elements that are themselves three-component vectors. The vector elements are identical apart from propagation delays Δ_j, defined in equation 3. The beam on three-component elements is obtained with a slight modification of the operation in equation (4):

$$b(t) = \frac{1}{N}\sum_{j=1}^{N} \boldsymbol{\gamma}^T \mathbf{r}_j(t+\Delta_j) \tag{22}$$

The beam consists of projecting the individual three-component waveforms onto the desired polarization vector (thus obtaining a scalar waveform), followed by shift-and-delay summing as in equation (4). This operation can be shown to be the maximum likelihood estimate of the signal in the case that the signal is a plane wave with the indicated polarization superimposed upon uncorrelated white noise. In the event that the background contains correlated noise or competing undesired signals from other seismic events, an extension of the adaptive beamforming technique described in the last section to polarized signals can be employed. An example will be discussed later in the report wherein we attempt to suppress signals from a seismic swarm in favor of signals from a single event in the Zagros mountains.

2. Objectives

A seismic array differs from a local network of seismic stations mainly by the techniques used for data analysis. Thus, in principle, a network of seismic stations can be used as an array, and data from an array can be analyzed as from a network. However, most array processing techniques require high signal coherency across the array, and this puts important constraints on the array geometry, spatial extent, and data quality. Furthermore, proper analysis of array data is dependent on a stable, high precision relative timing of all array elements. This is required because the measurement of (usually very small) time differences of the arrival of seismic signals between the different sensors plays an important role in all array-processing techniques.

Currently, no seismic arrays exist in the Arabian Peninsula. This project will provide research opportunities to collect new data from a modern three-component, broadband seismic array. Researchers and graduate students will be able to learn conventional array signal processing using data collected by this project. We will also enable next-generation array processing methods using coherent processing, such as match-field methods. This project will result in improved event detection and location capabilities by including array measurements.

Therefore, this proposal seeks to deploy a small-aperture (~ 3.5 km) three-component array in Saudi Arabia. The objective of this project is to collect and analyze continuous three-component waveform data with a seismic array in Saudi Arabia. The analysis will include characterization of background noise characteristics, signal characteristics and slowness-azimuth-polarization behavior of regional and teleseismic signals.

We extracted waveforms from reported seismic events from catalogues provided by the Saudi Geologic Survey (SGS) and King Abdulaziz City for Science and Technology (KACST). We performed conventional slowness-azimuth analysis as well as process three-component array data using methods to continuously measure polarization. This will be especially important for characterizing regional phases (Pn, Pg, Sn, Lg) that propagate in the crustal waveguide and upper-most mantle and for characterizing non-stationary background noise in order to design new algorithms for noise rejection.

We will also performed analysis of slowness and azimuth measurements to search for dipping layers, such as the Moho, and/or anisotropy. This analysis relies on previous reports of crustal and uppermost mantle structure. Waveforms from reported events were also used as templates for coherent processing, such as match-filter processing to improve detection performance.

3. Geologic and Seismotectonic Setting

The Arabian Peninsula forms a single tectonic plate, the Arabian Plate. It is surrounded on all sides by active plate boundaries as evidenced by earthquake locations. Figure 9 shows a map of the Arabian Peninsula along with major tectonic features and earthquake locations. Active tectonics of the region are dominated by the collision of the Arabian Plate with the Eurasian Plate along the Zagros and Bitlis Thrust systems, rifting and seafloor spreading in the Red Sea and Gulf of Aden. Strike-slip faulting occurs along the Gulf of Aqabah and Dead Sea Transform fault systems. The great number of earthquakes in the Gulf of Aqabah pose a significant seismic hazard to Saudi Arabia. Large earthquakes in the Zagros Mountains of southern Iran may lead to long-period ground motion in eastern Saudi Arabia.

The accretionary evolution of the Arabian plate is thought to have originated and formed by amalgation of five Precambrian terranes. These are the Asir; Hijaz, and Midyan terranes from the western part of the Arabian shield, and from the eastern side of the shield are the Afif terrane and the Amar arc of the Ar Rayn micro-plate. The western fusion is along the Bir Umq and Yanbu sutures (Loosveld et al 1996). The eastern accretion may have started by about 680-640 million years ago (Ma) when the Afif terrane collided with the western shield along the Nabitah suture. At about 670 Ma, a subduction complex formed west of Amar arc. Along this subduction zone, the Afif terrane and Ar Rayn microplate collided that lasted from about 640-620 Ma. (Al-Husseini 2000). The north trending Rayn anticlines and conjugate northwest and northeast fractures and faults may have formed at this time (Figure 10).

The Arabian Shield is an ancient land mass with a trapezoidal shape and area of about 770,000 sq. km. Its slightly-arched surface is a peneplain sloping very gently toward the north, northeast, and east. The framework of the shield is composed of Precambrian rocks and metamorphosed sedimentary and intruded by granites. The fold-fault pattern of the shield, together with some stratigraphic relationships suggests that the shield have undergone two orogenic cycles.

To the first order, the Arabian shield is composed of two layers, each about 20 km thick, with average velocities of about 6.3 km/s and 7 km/s respectively (Mooney et al 1985). The crust thins rapidly to less than 20 km total thickness at the western shield margin, beyond which the sediments of the Red Sea shelf and coastal plain are underlain by oceanic crust.

The platform consists of the Paleozoic and Mesozoic sedimentary rocks that unconformably overlays the shield and dip very gently and uniformly to the E-NE towards the Arabian Gulf (Powers et al., 1966). The accumulated sediments in the Arabian platform represent the southeastern part of the vast Middle east basin that extend eastward into Iran, westward into the eastern Mediterranean and northward into Jordan, Iraq and Syria.

The Arabian shield isolated the Arabian platform from the north African Tethys and played an active paleogeographic role through gentle subsidence of its northern and eastern sectors during the Phanerozoic, allowing almost 5000 m of continental and marine sediments deposited over the platform. This accumulation of sediments represents several cycles from the Cambrian onward, now forms a homocline dipping very gently away from the Arabian shield.

Several structural provinces can be identified within the Arabian platform : 1) An interior homocline in the form of a belt, about 400 km wide, in which the sedimentary rocks dip very gently away from the shield outcrops. 2) An interior platform, up to 400 km wide, within which the sedimentary rocks continue to dip regionally away from the shield at low angles. 3) Intra-shelf depressions, found mainly around the interior homocline and interior platform .

The Saudi Arabian Broadband Deployment (Vernon and Berger, 1997; Al-Amri et al., 1999) provided the first broadband recordings for the Arabian Shield and Platform. This deployment consisted of 9 broadband, three-component seismic stations along a similar transect to a seismic refraction study (Mooney et al., 1985; Gettings et al., 1986; Badri, 1991). Data from this deployment resulted in several reports of crustal and upper mantle structure (Sandvol et al., 1998; Mellors et al., 1999; Rodgers et al., 1999; Benoit et al., 2003; Mokhtar et al., 2001). The crustal model of the western Arabian Platform shows a slightly higher P-velocity for the upper crust in the Arabian Shield than in the Platform. Also the crust of the Platform appears to be 3-5 km thicker than in the Shield. The Moho Discontinuity beneath the western Arabian Platform occurs at a depth of 40-45 km, and the velocity of the upper mantle is about 8.2 km/sec (Al-Amri 1998; 1999; Rodgers et al., 1999; Tkalcic et al., 2006).

Generally, the crustal thickness in the Arabian Shield varies from about 15 km in the Red Sea, to 20 km along the Red Sea coast to about 35-40 km in the in central Arabian Shield (Sandvol et al., 1998; Al-Damegh et al., 2005; Tkalcic et al., 2006). Reports of large-scale seismic tomography (e.g. Debayle et al., 2001) suggest that a low-velocity anomaly in the upper mantle extends laterally beneath the Arabian Shield from the Red Sea in the west to the Shield-Platform boundary in the east. Additionally, Debayle et al. (2001) observed a narrow region of low-velocity beneath the Red Sea and the western edge of the Arabian Shield, extending to 650 km depth. Recent tomographic imaging by Park et al. (2007) using SANDSN data found low velocities extending to 400 km in the upper mantle beneath the southern Red Sea and Arabian Shield, but more normal velocities beneath the northern Red Sea, suggesting different geodynamic connections between rifting of the Red Sea and mantle upwelling in the southern and northern Red Sea.

High-frequency regional S-wave phases are quite different for paths sampling the Arabian Shield than those sampling the Arabian Platform (Mellors et al., 1999; Al-Damegh et al., 2004). In particular the mantle Sn phase is nearly absent for paths crossing parts of the Arabian Shield, while the crustal Lg phase has abnormally large amplitude. This may result from an elastic propagation effect or extremely high mantle attenuation and low crustal attenuation occurring simultaneously, or a combination of both. High-frequency Lg does not propagate as efficiently across the Arabian Platform compared to the Shield but Sn does propagate efficiently. This suggests that crustal attenuation is low in the higher velocity crust of the Arabian Shield, or sedimentary structure in the Arabian Platform attenuates and disrupts the crustal waveguide for Lg. These observations imply high-frequency ground motions will propagate with lower attenuation in the Arabian Shield compared to the Arabian Platform.

It is known that high-frequency regional phase behavior in the Arabian Plate is quite variable as demonstrated by Al-Damegh et al. (2004). They investigated the attenuation of *Pn* phase (Q_{Pn}) for 1–2 Hz along the Red Sea, the Dead Sea fault system, within the Arabian Shield and in the Arabian Platform. Consistent with the

Sn attenuation, they observed low Q_{Pn} values of 22 and 15 along the western coast of the Arabian Plate and along the Dead Sea fault system, respectively, for a frequency of 1.5 Hz. Higher Q_{Pn} values of the order of 400 were observed within the Arabian Shield and Platform for the same frequency. Their results based on *Sn* and *Pn* observations along the western and northern portions of the Arabian Plate imply the presence of a major anomalously hot and thinned lithosphere in these regions that may be caused by the extensive upper mantle anomaly that appears to span most of East Africa and western Arabia.
More recently, Pasyanos et al. (2009) applied a technique to simultaneously invert amplitudes measurements of Pn, Pg, Sn and Lg to produce P-wave and S-wave attenuation models of the crust and upper mantle. The attenuation is modeled as P-wave and S-wave attenuation surfaces for the crust, and similar set for the upper mantle. They used all of the phase amplitudes together by using the appropriate (source, geometrical-spreading, site, and attenuation) terms for each phase. Because this is a model-based inversion, the velocity structure of the region can be included to more accurately model the predicted raypaths (Fig. 11).

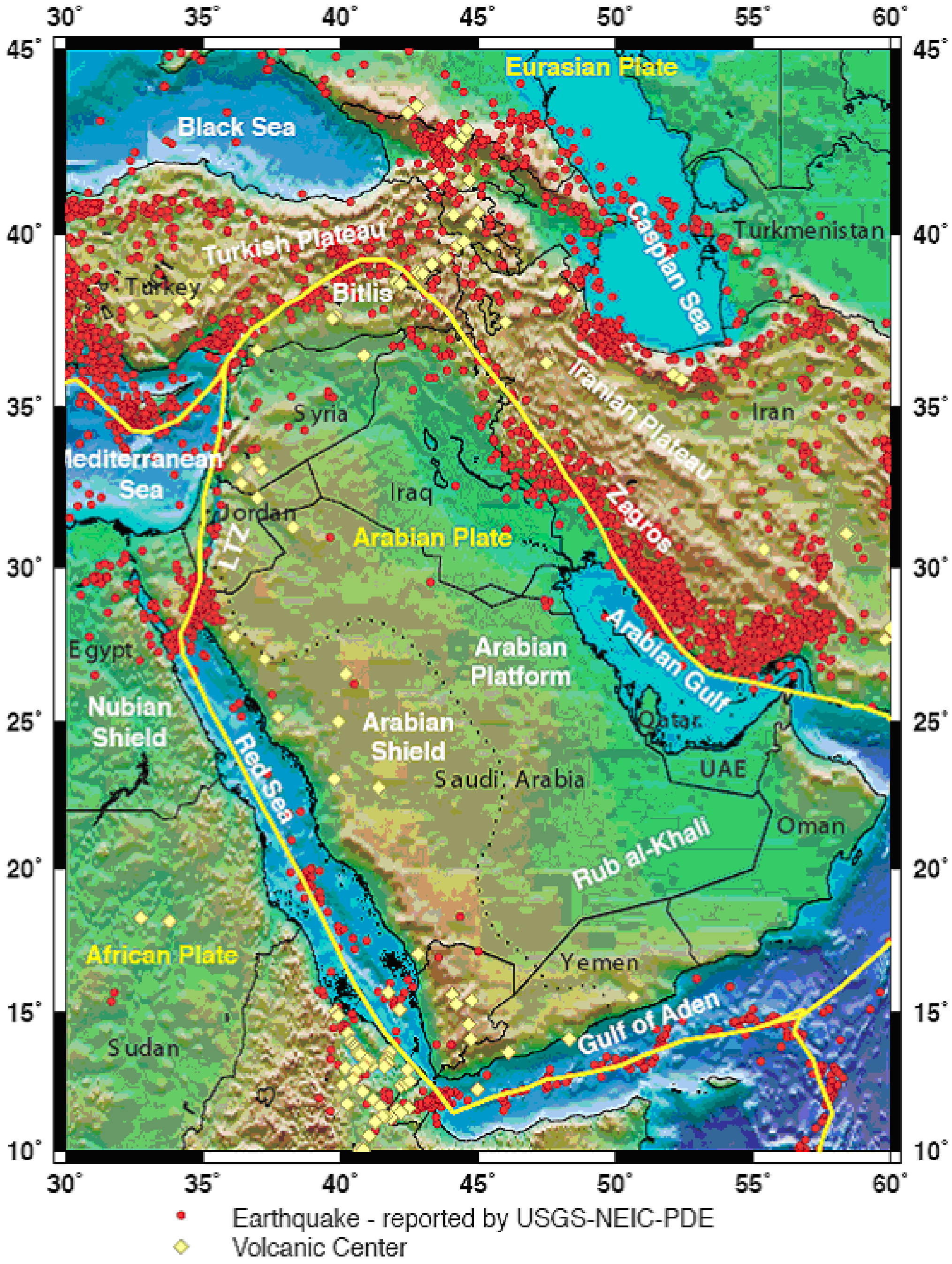

Figure 9 Seismotectonic map of the Arabian Peninsula and Arabian plate boundaries.

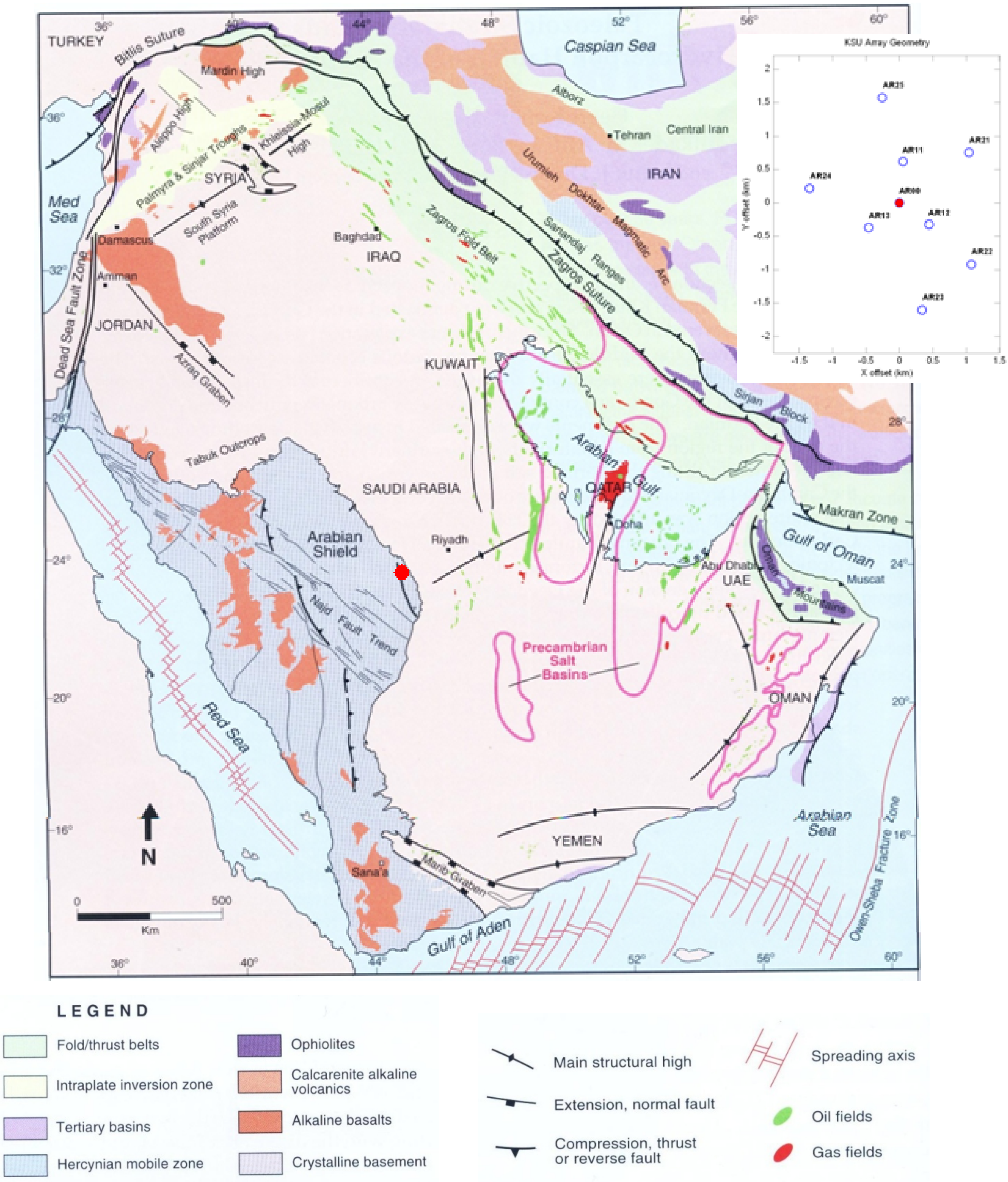

Figure 10 Location map of the Arabian Plate showing major tectonic elements of the Arabian Shield and Platform (Al-Husseini, 2000). The red dot near the edge of the Arabian Shield denotes the array location.

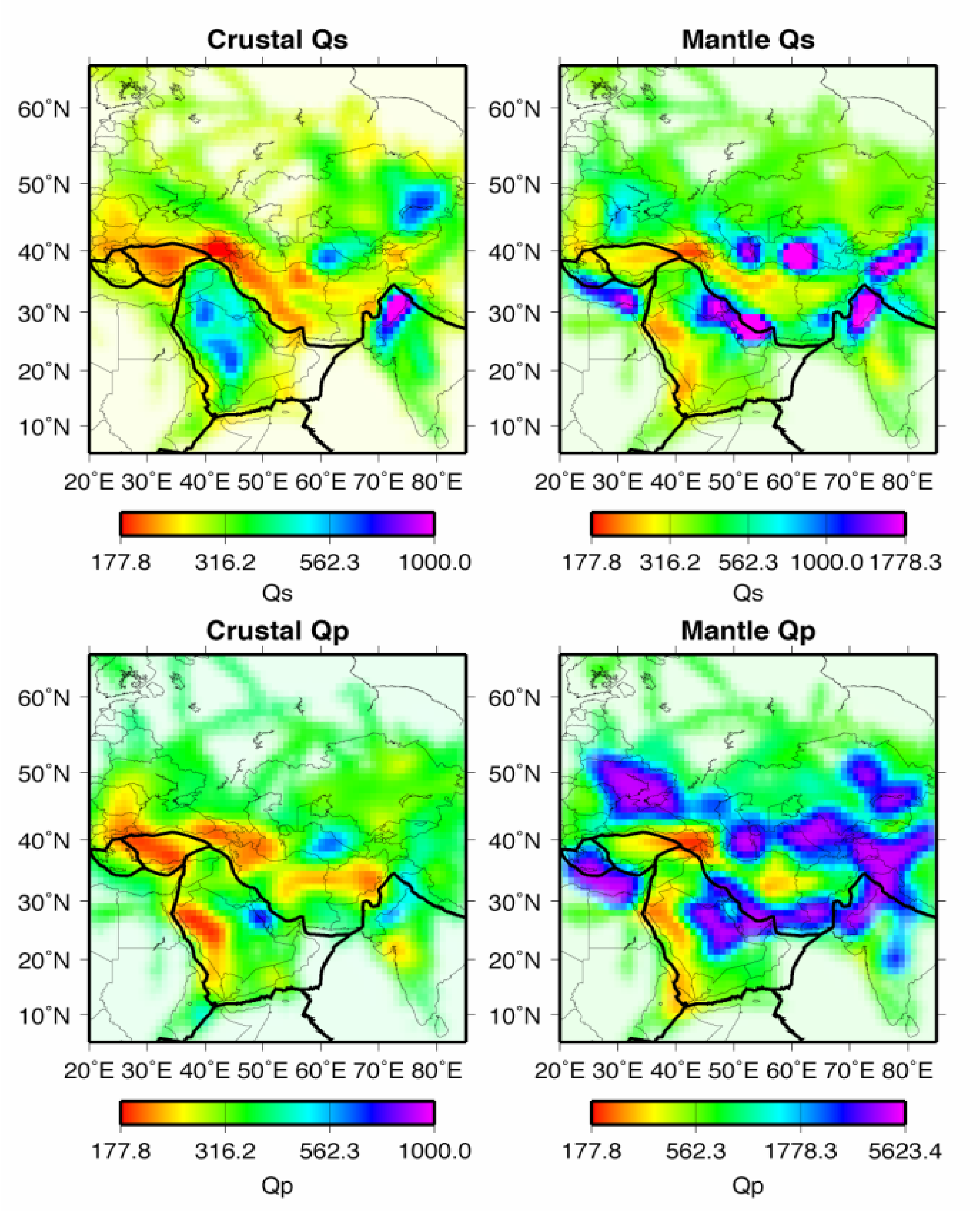

Figure 11 Maps of attenuation quality factor Q for shear waves in the crust (crustal Qs), shear waves in the mantle (mantle Qs), compressional waves in the crust (crustal Qp), and compressional waves in the mantle (mantle Qp) in the 1-2 Hz passband. (Pasyanos et al., 2009b).

4. Methods & Materials

The Ar Rayn array was deployed in late 2009 and consisted of a central broadband element (Figure 12) surrounded by eight short-period stations. It follows the classic short-period array design [Mykkeltveit et al. 1983, 1990a,b, Followill and Harris, 1983] for regional event detection, phase identification and backazimuth estimation, and is quite similar to many of the IMS arrays deployed since 1995. The aperture of the array is about 3.5 kilometers, and minimum element spacing is about 500 meters. These design parameters make the array most suitable for detection and estimation problems involving regional phases in the short-period band.

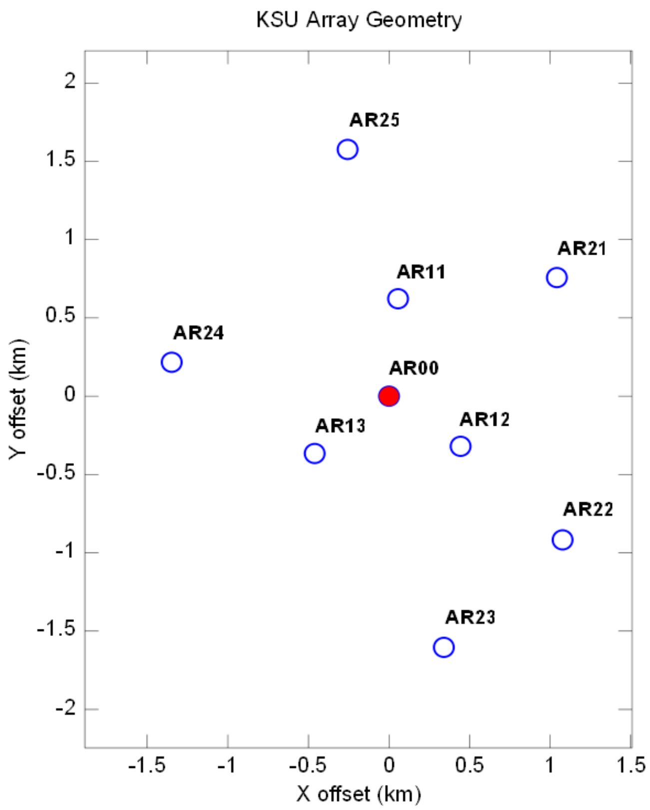

Figure 12 The Ar Rayn seismic array has a broadband (STS-2) three-component sensor at its central location(filled circle) surrounded by two rings of three-component short-period (SS-1 Ranger) sensors.

4. 1 Installation

Great care was taken to site the stations of the Ar Rayn array on Precambrian outcrops. Figure 13 shows a representative station site (AR25). Note that the station is sited adjacent to an outcrop where it was possible to excavate a vault into contact with undisturbed Precambrian bedrock. The inside dimensions of the vault are 1.6 meters square and 2 meters deep (Figure 14). At the bottom a 1.4 meter by 1.4 meter concrete pier, 20 centimeters thick, was poured directly on bedrock. This dimension affords a 10 cm separation between the pier and the walls of the vault for noise isolation. The walls themselves are composed of two shells, a concrete block wall on the outside, with foam filling the voids of the blocks for thermal isolation, and a 20 cm inside wall poured of solid concrete. Neither of the walls contains any steel reinforcement to prevent possible noise contributed to the motion of the mass. The top of the vault is covered by a double door with 10 cm of foam for thermal isolation. The walls and top of the vaults are flush with the ground surface to minimize wind noise. The 80 watt solar panel is mounted close to the ground surface also to minimize wind noise that would be transmitted into the vault had a mast mounting been used.

The short-period instruments are Kinemetrics SS-1 Ranger seismometers (one Hz free period). Three are arranged in a three-component configuration as shown in Figure 14. The data are acquired by Quanterra Q330 data loggers and stored on Belar 44 data storage devices with thirty-two gigabytes of flash memory. The sampling rate is 100 samples per second for each channel. The single broadband sensor at the center of the array (AR00) is a Streckheisen STS-2. Otherwise the configuration of this installation is the same as the short-period stations.

Figure 13 Stations sites were chosen for Precambrian bedrock contact

Figure 14 Typical vault installation of a short period three-component instrument. The concrete pier was poured on bedrock.

4.2 Noise Level at the Site

Figure 15 shows noise level as a function of frequency for the three components of the broadband center element of the array, and follows the format of Astiz (1997). The vertical axis is acceleration power expressed in decibels with respect to 1 $m^2/s^4/Hz$. The grey lines denote the USGS low and high noise models of Peterson (1993). The methodology of this noise estimate differs from that used to determine the USGS low- and high-noise models and consequently absolute power levels may differ slightly due to bias induced by different tapers and windows. At mid- and higher frequencies, the three noise spectra lie near the USGS low noise model departing somewhat above 2 Hz. The high frequency noise, especially the distinct spectral lines, could be instrument noise or cultural noise from the nearby town of Ar Rayn, which is 15 kilometers from the array.

In general, noise levels are similar for all channels for frequencies greater than 1 Hz. Between 1 Hz and roughly 0.1 Hz, the vertical is slightly noisier than the horizontals. At frequencies less than 0.1 Hz, the horizontal components are much noisier, creating an obvious discrepancy with the low-noise-model. The long-period noise levels on the horizontal channels may present a problem for surface wave studies and regional moment tensor inversions, which are forced to depend solely on vertical data for moderate sized events. The source of the noise is not clear. One possibility is that the long period noise may be due to small tilts which affect the horizontal more than the verticals because horizontal tilts greatly increase the effect of the local gravity vector. Tilt effects can be quite large compared to the signals normally recorded, and may be due to prevailing winds and/or transient thermal effects caused by large diurnal temperature variations in the desert.

The body-wave magnitude (mb) detection threshold for the distance range of 10-100 degrees is about m_b >3.5 (Vernon and Berger, 1997). Minimum detectable magnitudes are estimated for RAYN station using the observed noise levels over 1 Hz. The m_b detection threshold for the distance range of 5-10 degrees is about 2.7-3.0 assuming the signal-to-noise ratio of 3 dB or better (Al-Amri et al., 1999). They indicated that seasonal noise levels varied at RAYN, with April to June being the quietest and with October to December being the nosiest months. Slight changes in peak microseism frequency also occurred seasonally. Absolute noise levels near the microseism frequency (0.1 to 0.2 Hz) were about equal for all seasons at -140 dB. Above 1Hz, RAYN station shows an increase in seasonal variations from -140 dB in the summer to -160 dB in the winter. Mellors (1997) showed that noise levels at nine broadband stations (STS-2) across the Arabian Shield are similar for all channels for a given station for frequencies greater than 0.9 Hz. Between 0.9 Hz and roughly 0.1 Hz, the vertical is slightly noisier than the horizontals, and at frequencies less than 0.1 Hz, the horizontals are much noisier.

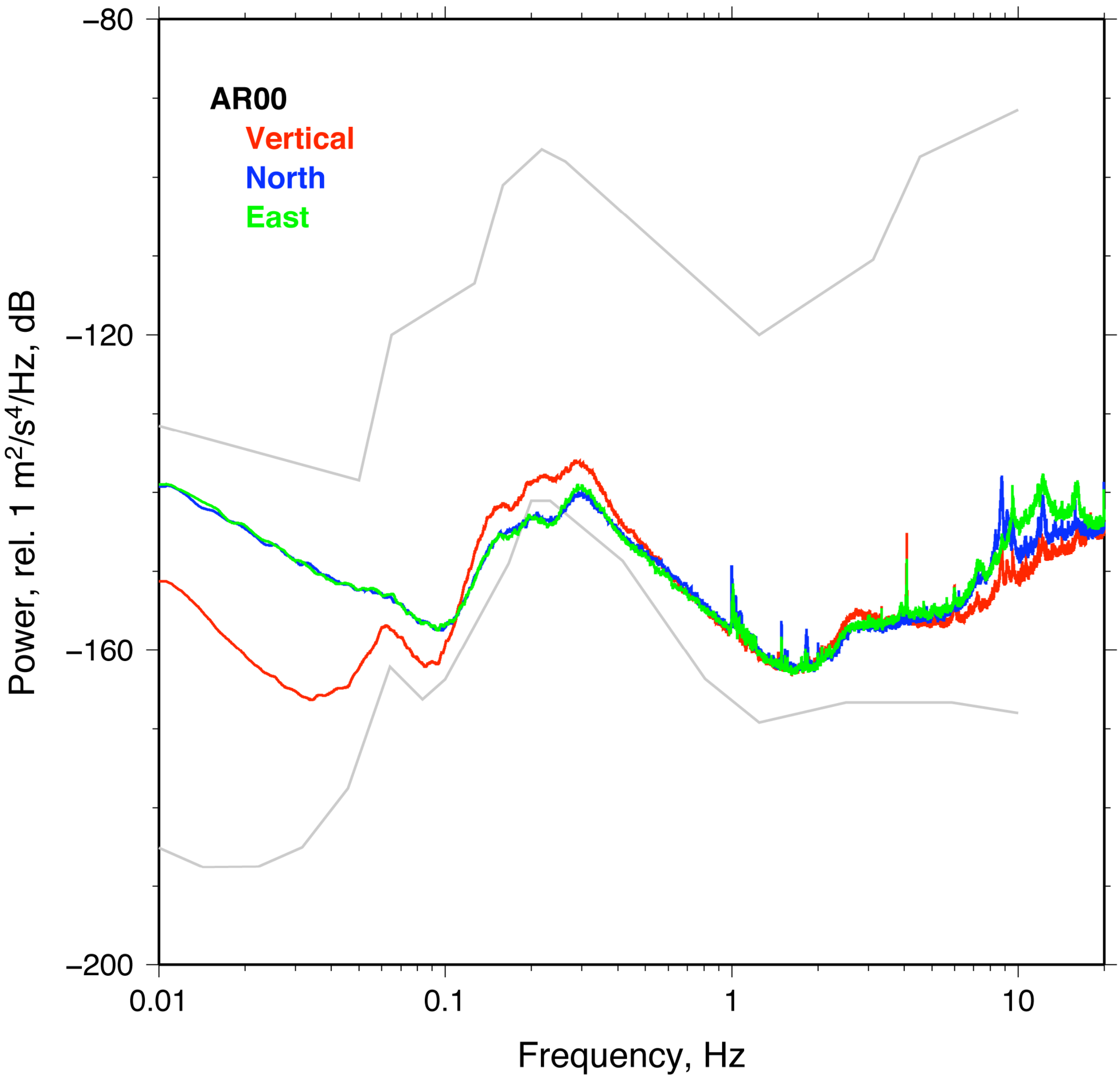

Figure 15 Average ambient noise levels for the three components of the central broadband element AR00 (vertical, north and east as red, blue and green, respectively). The noise power spectral densities are expressed in acceleration power relative to 1 m**2/s**4/Hz in decibels (dB). Reported low and high noise models from Peterson (1993) are shown as gray curves. The noise levels are quite low, near the USGS low noise model for the central band of 0.05 – 10 Hz. Noise levels increase from the low noise model away from the central frequencies. Sharp noise spikes are apparent at 1.0 and 4.0 Hz in all channels. These could be instrumentation noise or cultural noise from the nearby town of Ar Rayn, which is 15 kilometers distant.

4.3 Coherence

As outlined in the introduction array signal processing crucially depends on a plane wave model for the incident seismic waves, which, in turn, requires that signals observed across the array be identical apart from propagation delays. The choice of sites and technique of installation must be such as to satisfy this requirement. Whether the installation was successful can be determined from a check of coherence among signals that are expected to be highly similar. For a small-aperture array this is most readily accomplished by measuring the coherence of a teleseismic arrival. Teleseismic P waves arrive at a steep angle of incidence and have most of their energy in a low frequency band, typically around 1-3 Hz. Because the ray paths from the source to the station are so similar and traverse deeper portions of the mantle, where scattering is less pronounced than in the crust and upper mantle, the observed signals are anticipated to be highly similar.

We conducted a check of coherence using a teleseismic observation of an m_b 5.3 earthquake (Fig. 16) in the vicinity of Greece (USGS preliminary hypocenter 38.425 N and 44.022 E, depth 10 km) that occurred on January 22, 2010 at 00:46:57.5 GMT. Figure 17 (left) displays the vertical waveforms of seven of the array short-period elements in a 30-second window about the initial P phase filtered in the 1-3 Hz band. The right part of the figure shows an FK spectrum computed from that P phase. The back-azimuth (-63.4 degrees) and phase velocity (10.2) values estimated from the spectral peak were used to align the signals for a coherence analysis. That analysis is shown in Figure 18, with the aligned P waveforms on the top and, on the bottom, the correlation values of all 21 distinct pairs of signals plotted as a function of sensor separation. The correlation values are quite high, as is expected for a low-frequency teleseismic P phase observed across a 3 kilometer aperture. Nonetheless, the high correlation values indicate desirable uniformity of vault installation, coupling to bedrock, site response and instrumentation.

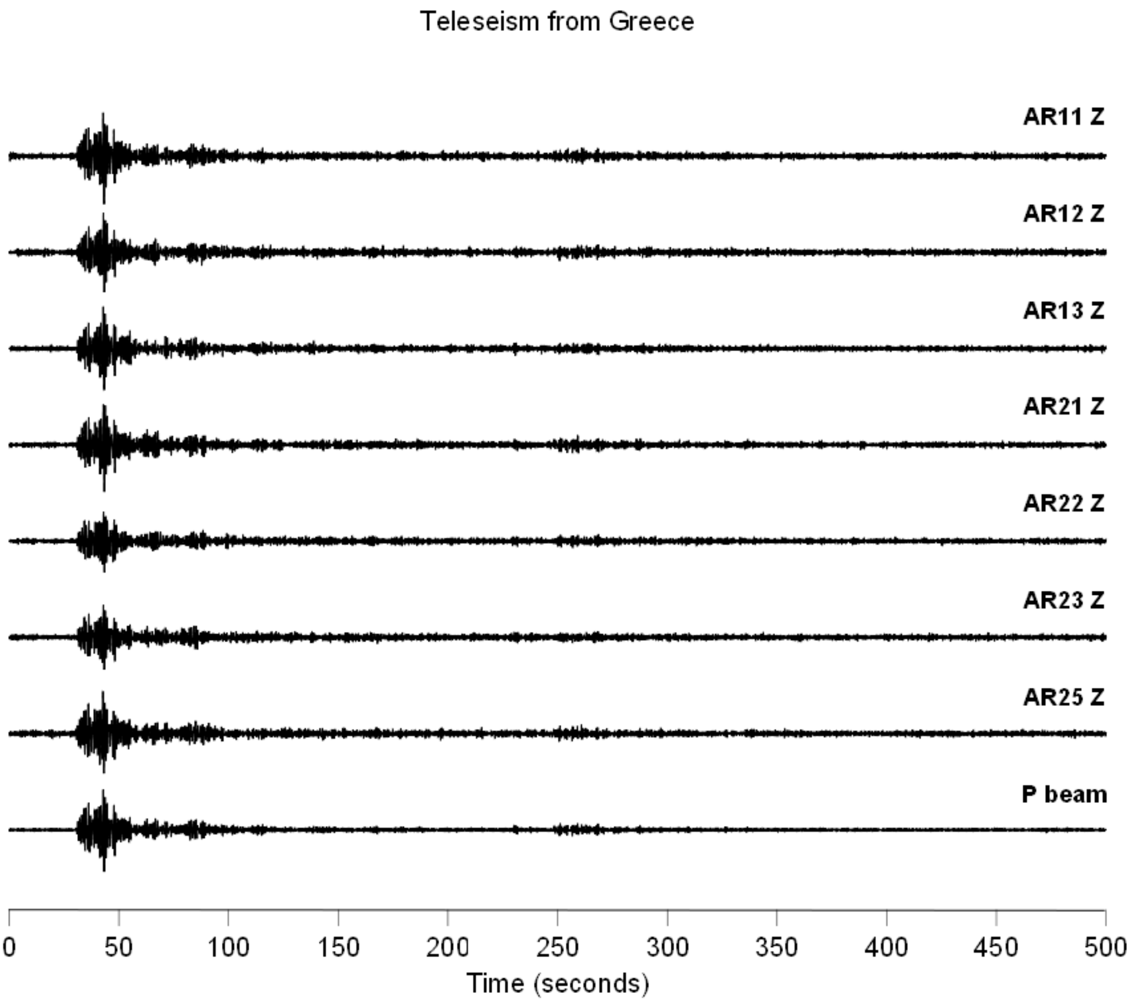

Figure 16 Teleseismic P wave from an event near Greece recorded on 7 sensors of the array. The beam at the bottom of the plot is steered to the direction and velocity of the initial P wave, and indicates a weak P arrival (PcP?) about 250 seconds into the plot.

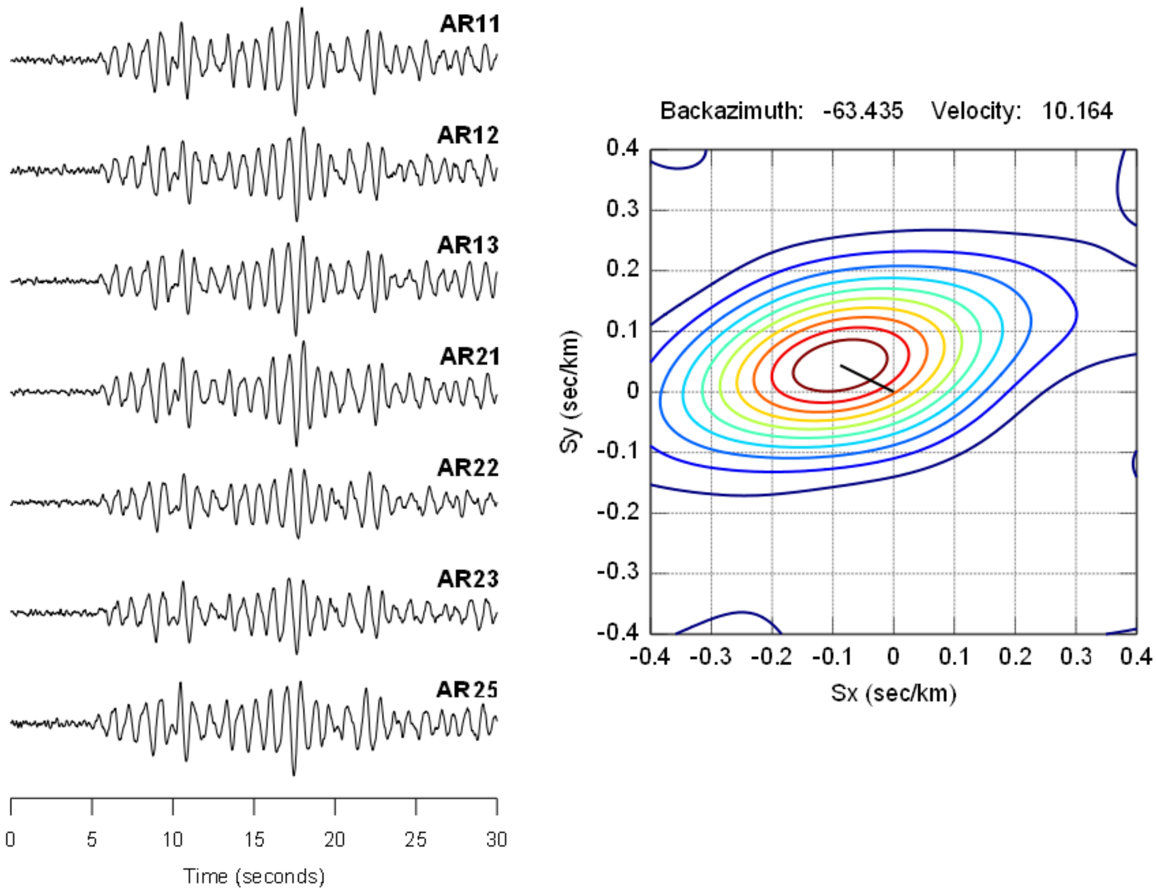

Figure 17 FK spectrum, computed between 1 and 3 Hz, of the initial P phase for the event of Figure 10. The cut P phase waveforms are shown at left, and the FK spectrum to the right. Coherence of this near phase is high as is expected of a teleseismic observation; the measured backazimuth and phase velocity are used to align the waveforms for a coherence measurement.

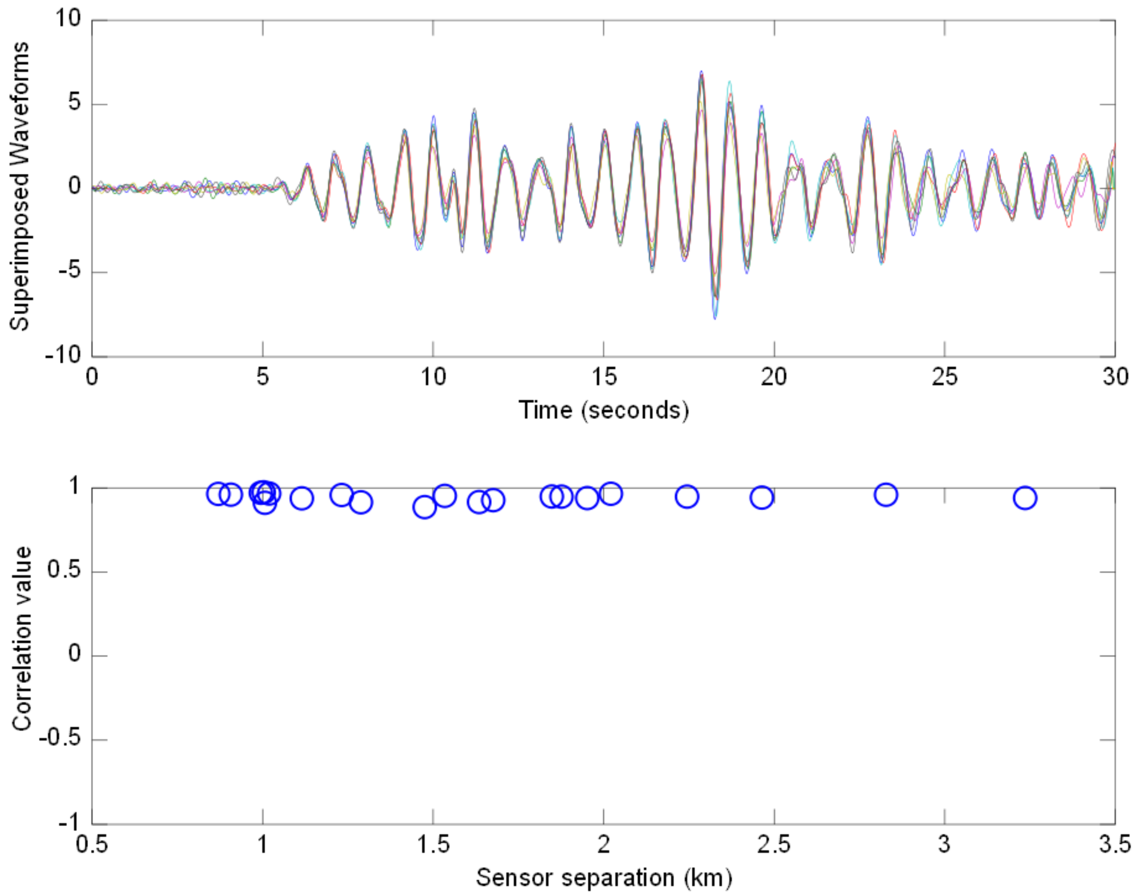

Figure 18 Coherence of the teleseismic P phase at the array is high, demonstrating uniformity of installation and instrumentation. At top, the first 25 seconds of the P wave of the teleseism from Greece are superimposed after being shifted to align them to the back-azimuth and velocity obtained with FK analysis. At the bottom, the 21 correlation coefficients between unique pairs of sensors are shown plotted as a function of sensor separation. The P phase is relatively narrowband, with most of its energy just above 1 Hz.

For combined beamforming and polarization analysis to function properly, the polarization properties of the wavefield must be unifrom over the array aperture. We test this assumption with an analysis of the polarization characteristics of a teleseismic P phase from an event in Central Asia (Figure 19). This was a magnitude 5.6 event that occurred on 18 April 2010 at 20:28:50 GMT. A data window containing the initial P is shown at left in Figure 20. The corresponding frequency-wavenumber (FK) spectrum is shown to the right in the figure. The frequency wavenumber spectrum is a map of the energy incident upon the array as a function of the horizontal slowness vector defined earlier, and serves to define the direction to the event (44 degrees in this case) and the horizontal velocity (reciprocal of the ray parameter; 8.6 km/sec in this case.

Principal component analysis was applied to this event using the 21 channels corresponding to the 7 three-component stations recording at the time (AR11, AR12, AR13, AR21, AR22, AR23, AR25). A covariance matrix was formed on the data window (augmented to include the horizontal waveforms) shown in Figure 20. The principal eigenvector was extracted, and the elements of the eigenvector were interpreted to estimate the local back-azimuth and incidence angles to the event for each station. The projections of the P polarization vectors onto the horizontal plane are shown in Figure 21. Note the considerable uniformity in the estimated back-azimuths across the array aperture. The consistent lengths of the vectors indicate a uniform angle of incidence (ray parameter) across the array. This example is evidence again of a desirable uniformity of array station installations and site characteristics.

Figure 19 Location of the Central Asian event used to verify consistency in P polarization across the array aperture. The path from this event to the Ar Rayn array is shown in red.

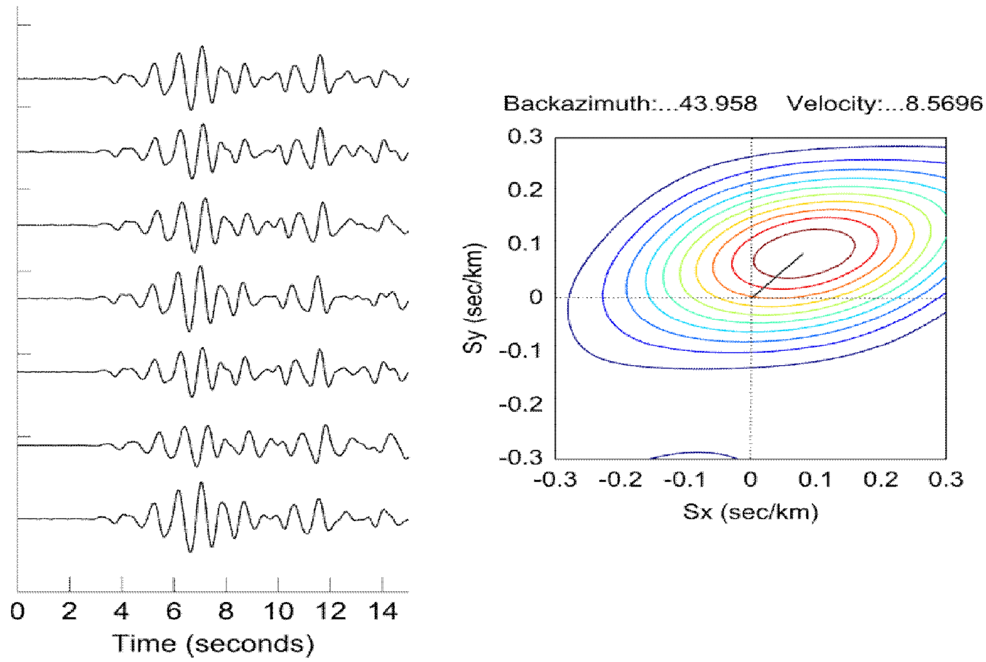

Figure 20 P waveforms and FK spectrum indicating observed backazimuth to the source.

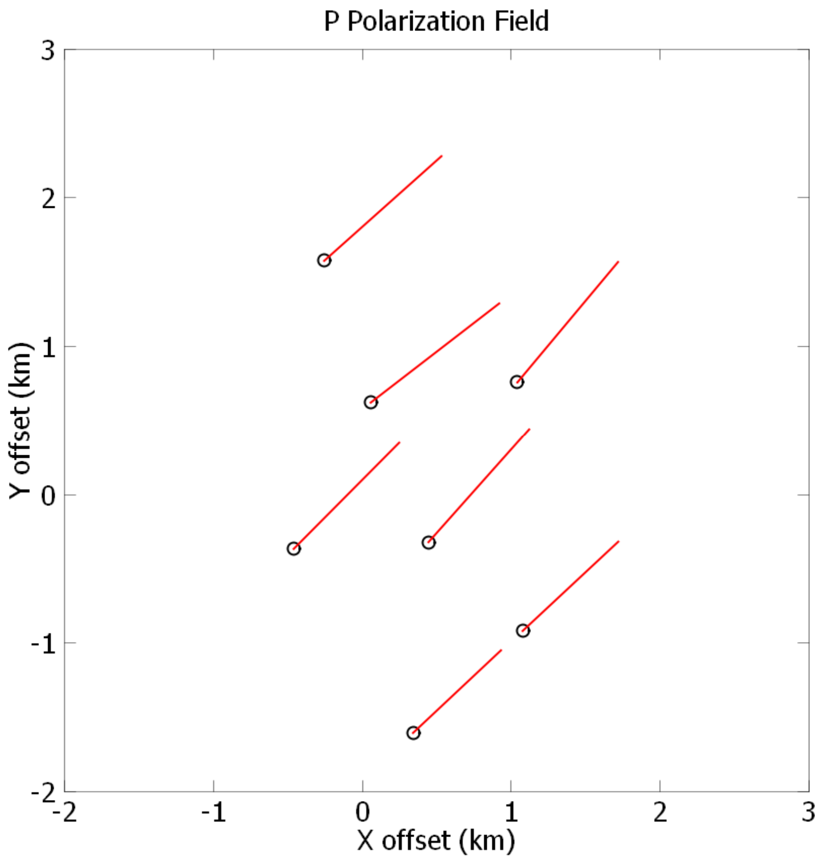

Figure 21 Polarization of the P phases is consistent across the Ar Rayn aperture. Here the direction of the polarization vector is indicated by its projection onto the horizontal plane. The consistency of the length of the vectors is evidence of the similarity of angles of incidence across the array.

5. Results & Data Processing

As the primary purpose of this project was to examine the ability of arrays to improve detection and interpretation of events within the Arabian Peninsula, we first examine beamforming and FK analysis for two such events.

5.1 Detection of Weak P in the Arabian Peninsula

An interesting observation of a local event is shown in Figures 22 through 24. This is a local magnitude 2.3 (KACST catalog) event which occurred approximately 260 kilometers NNE of the array. Only the Lg phase is clear in the data (Figure 22) filtered into the 0.8 to 3 Hz band. There is a hint of a P phase approximately 30 seconds before the Lg signal, but nothing that can be reliably picked for an arrival time. Higher frequency filter bands do not improve the signal to noise ratio in this case. A wideband (1-3 Hz) FK spectrum of the Lg arrival (Figure 23) provides a usable backazimuth and a phase velocity confirming the identity of the Lg phase. The measured Lg back-azimuth and an assumed phase velocity of 8 km/sec can be used to search for the P phase arrival. Figure 24 shows an individual vertical waveform (top trace) and the P beam (equation 4, middle trace). The (probable) Pn phase now is clearly visible. Still greater processing gain can be obtained for the P phase by combining beamforming and polarization filtering (equation 22). The third trace in the figure shows a polarized beam obtained by forming separate beams on the vertical, north and east components of the array, then rotating the resulting three-component beam set onto the polarization vector of Pn for this event (back-azimuth 29.5 degrees, angle of incidence 39 degrees). The angle of incidence used assumes a near-surface medium velocity of 5 km/s. This processing approach roughly doubles the signal-to-noise ratio of the incident P wave, enhancing our ability to pick and identify this phase.

Our second example is an extraction of crustal and upper mantle P phases for an event in the Harrat Lunayyir volcanic center (25.215N 37.796E), approximately 790 kilometers from the array. The event occurred on April 15, 2010 (04:10:04.25 GMT) and was estimated to be a magnitude 3.7 event by the Saudi Geological Survey. Figure 25 shows single channel recordings and beams for this event. The top trace is a vertical channel (station AR11) filtered into the 1-4 Hz band. A pronounced Lg phase is apparent, preceded by approximately 110 seconds by a very weak P phase. The three bottom traces in the figure are detailed views around the P phases, with the first of the three being again the filtered single vertical trace. The second trace is the beam formed from the vertical channels only, and the third trace is the three-component beam (equation 22). Note that, as with the smaller near-regional event, the three-component beam roughly doubles the power SNR for the Pn phase. Pg also is more clearly visible on this beam, arriving about 14 seconds after Pn.

These examples clearly demonstrate the value of small-aperture arrays for observing weak regional phases. Picks on Pn in the first case and Pg in the second would not be possible at this site without beamforming operations on the data.

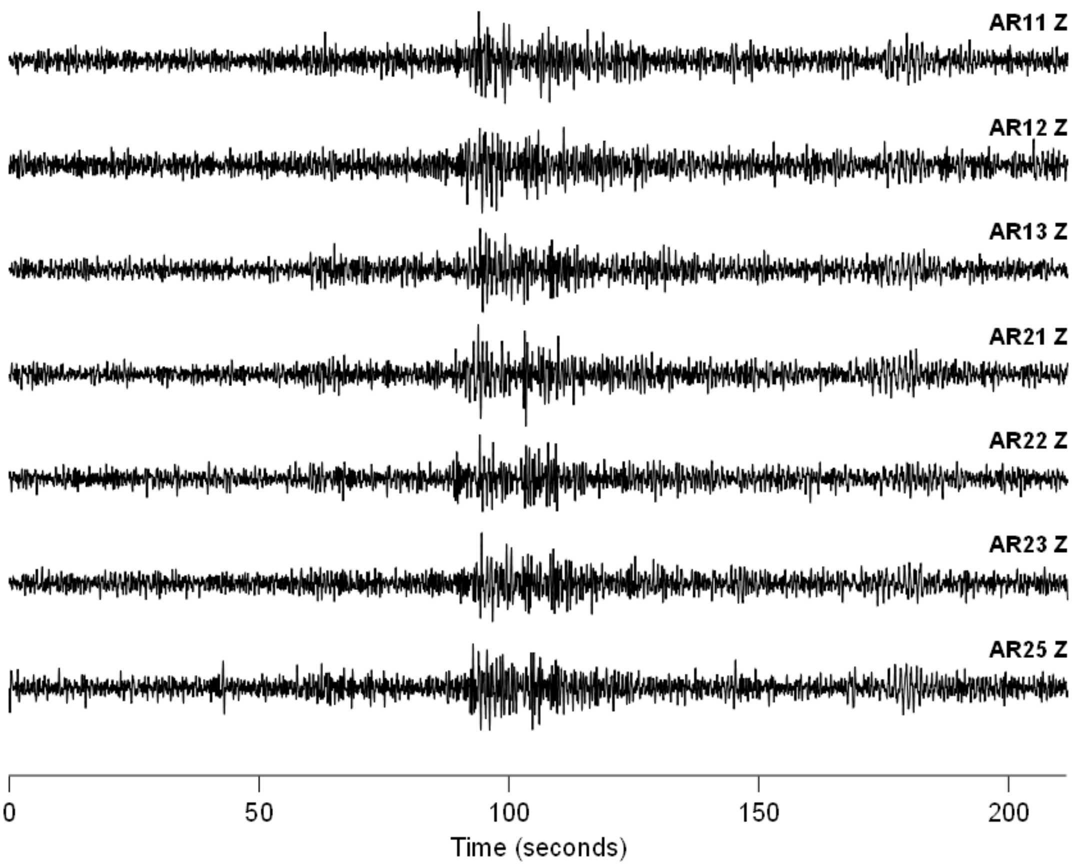

Figure 22 This small central Arabian event about 260 kilometers from the array has a low SNR that makes observation of the P phases difficult. A window around the Lg phase from 90 to 100 seconds allows backazimuth estimation with an FK spectrum.

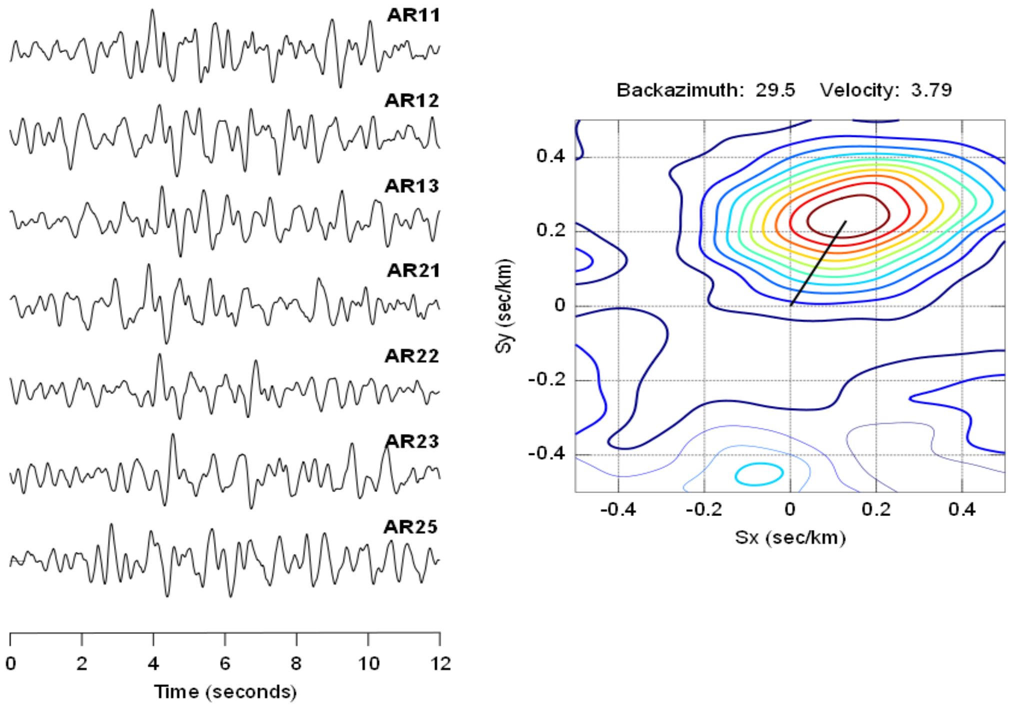

Figure 23 Lg phase window (left) and FK spectrum (right) used to obtain beamforming parameters (backazimuth) for the Pn beams.

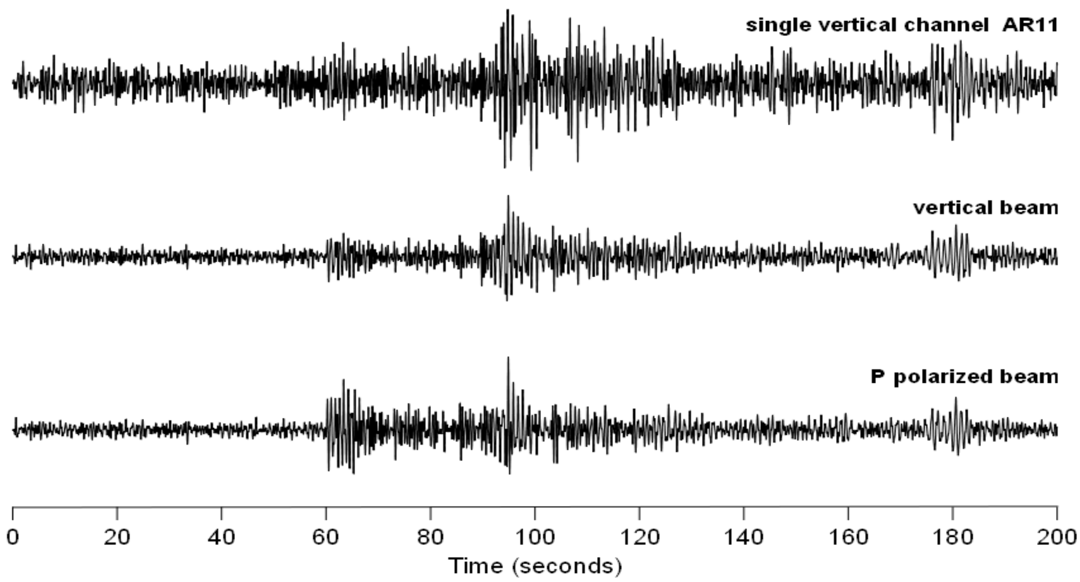

Figure 24 Single vertical channel (top trace), vertical beam (middle trace) and three-component beam (bottom trace) directed at the Pn phase for the central Arabian event.

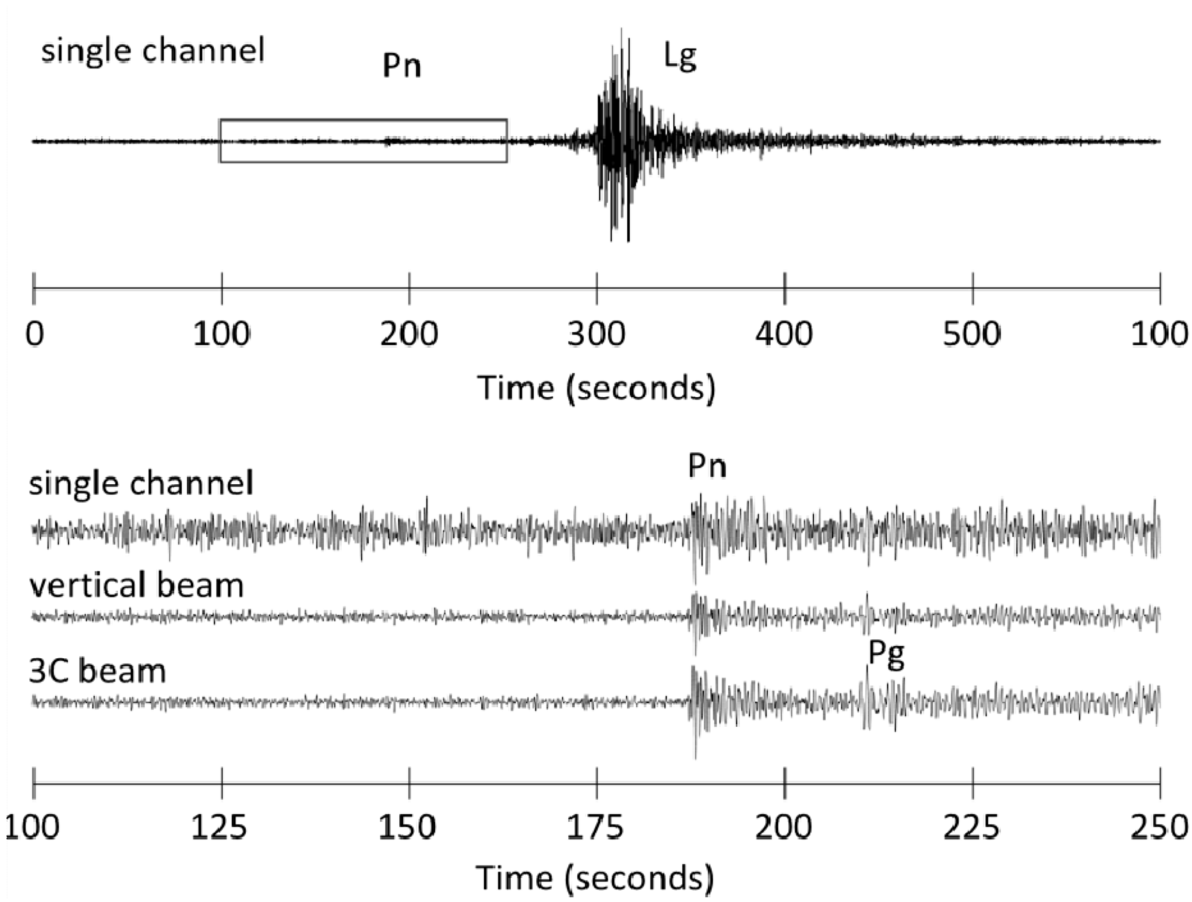

Figure 25 Example of beamforming for an event at Harrat Lunnayir. The top trace shows a single channel of the array filtered into the 1-3 Hz band. The bottom three traces show a smaller time interval around the initial P arrivals. Pn is just visible in the single channel trace. A beam of vertical channels only shows the onset of the Pn phase much more clearly. The three-component beam (bottom trace) roughly doubles the SNR of the Pn phase and also clearly displays Pg.

5.2 Detection of Regional Monitoring

The Ar Rayn array also performed well for detection of regional and near teleseismic events. Here we return to the example of the central Asian event located as shown in the map of Figure 19. This event had two aftershocks of magnitude 4.8 and 4.6 (NEIC) respectively. The weaker aftershock took place on 28 April 2010 at 21:37:25 GMT and the stronger aftershock on 19 April 2010 at 01:26:56 GMT. Figure 26 shows the P phases for the main event and the two aftershocks filtered into the detection band of 0.8-3 Hz. Note that the P phase of the magnitude 4.6 aftershock is barely discernable above the noise. We focus on extracting this phase as our demonstration of beamforming gain.

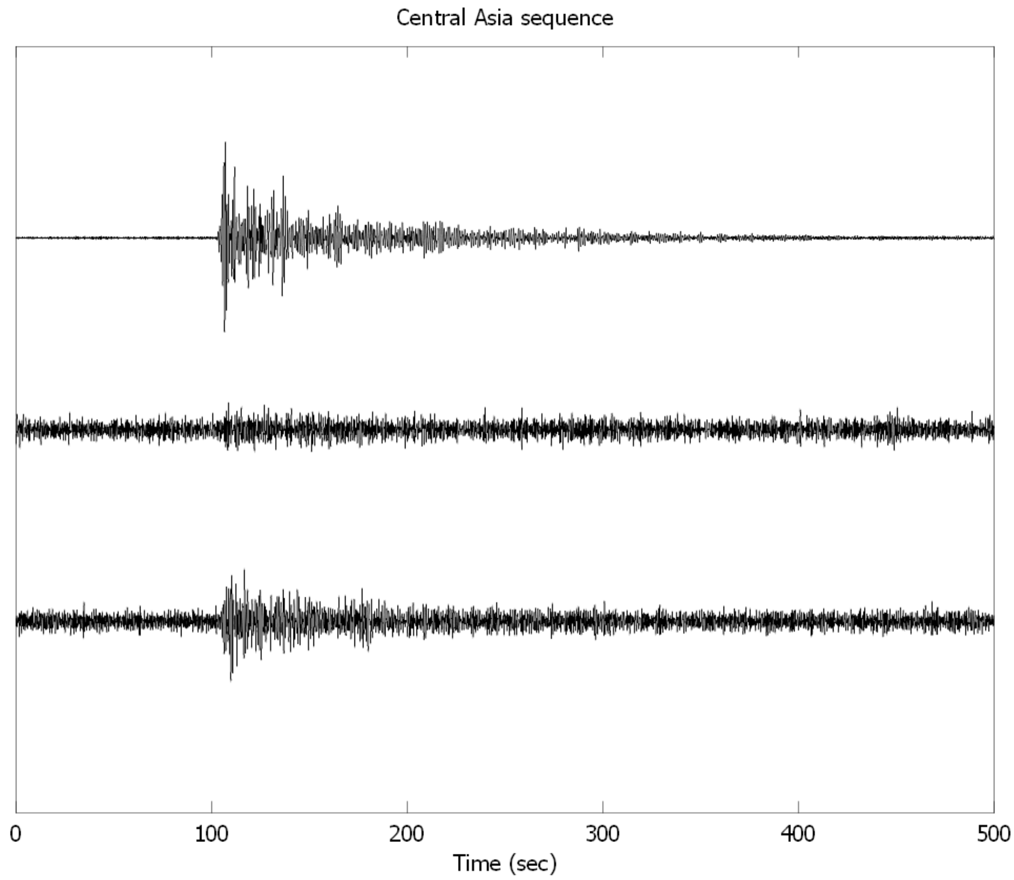

Figure 26 Representative P phases (0.8 - 3 Hz) for three Central Asian events. At top is an mb 5.6 event, followed by mb 4.6 (middle) and mb 4.8 (bottom) aftershocks. The two bottom traces have been multiplied by a factor of 10.

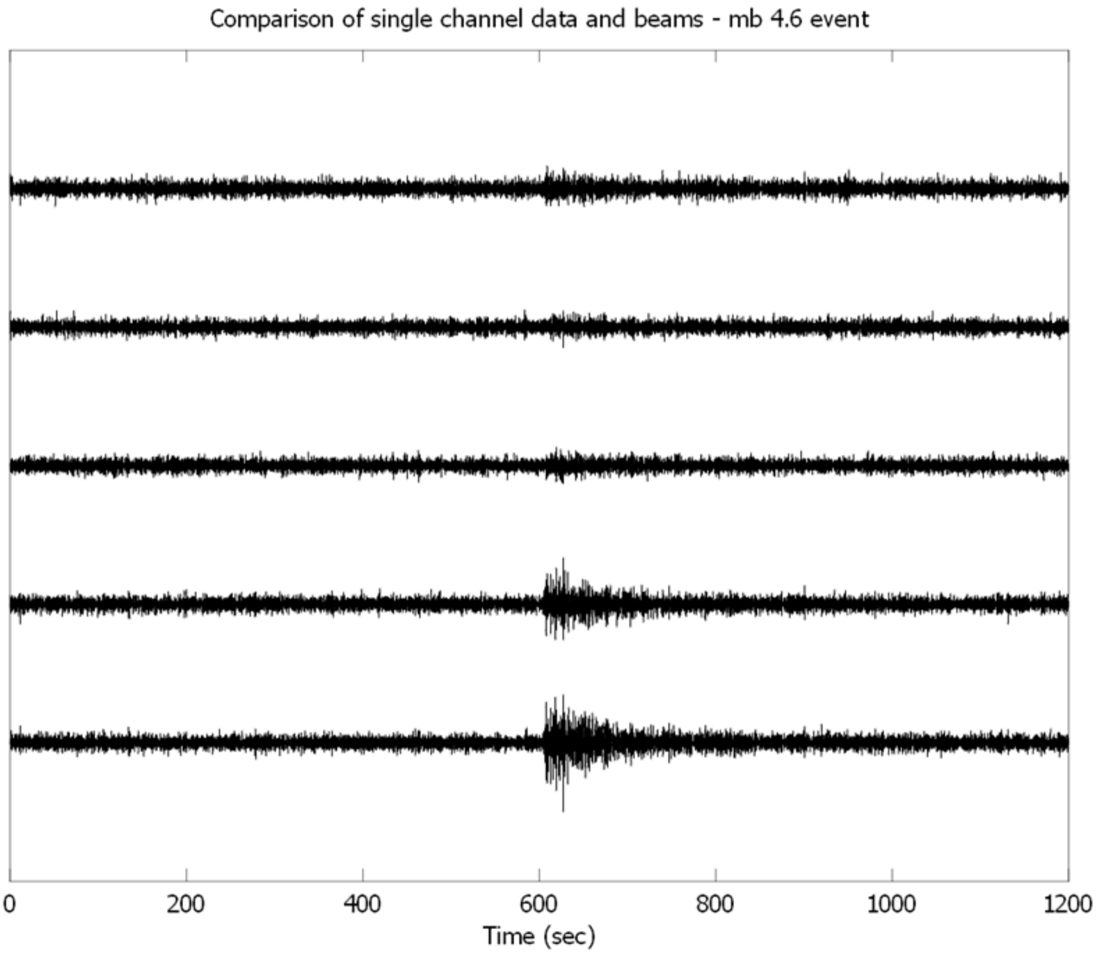

Figure 27 Comparison of individual channels (top 3 traces) and array beams (bottom 2 traces) for the magnitude 4.6 central Asia aftershock.

Using the backazimuth (44 degrees) and velocity (8.56 km/sec) obtained by FK analysis on the main event, we calculated vertical only (equation 4) and three-component (equation 22) beams on the data window containing the weak aftershock. The results are shown in Figure 27. The top three traces of the figure are individual channels of the array, confirming that the P phase is not detectable with confidence in the filtered raw data. The vertical-only beam is shown in the fourth trace, which clearly shows the teleseismic P phase. The bottom trace is the three-component beam, which shows the P phase even more clearly. Figure 28 shows the power envelopes of these two beams, which demonstrate that the P phase observation in the three-component beam has about twice the power SNR of its counterpart in the vertical-only beam. This performance is not quite as good as the near regional examples, which may be due to the fact that the near-regional phases have a larger projection onto the horizontal elements of the array, at least for P phases.

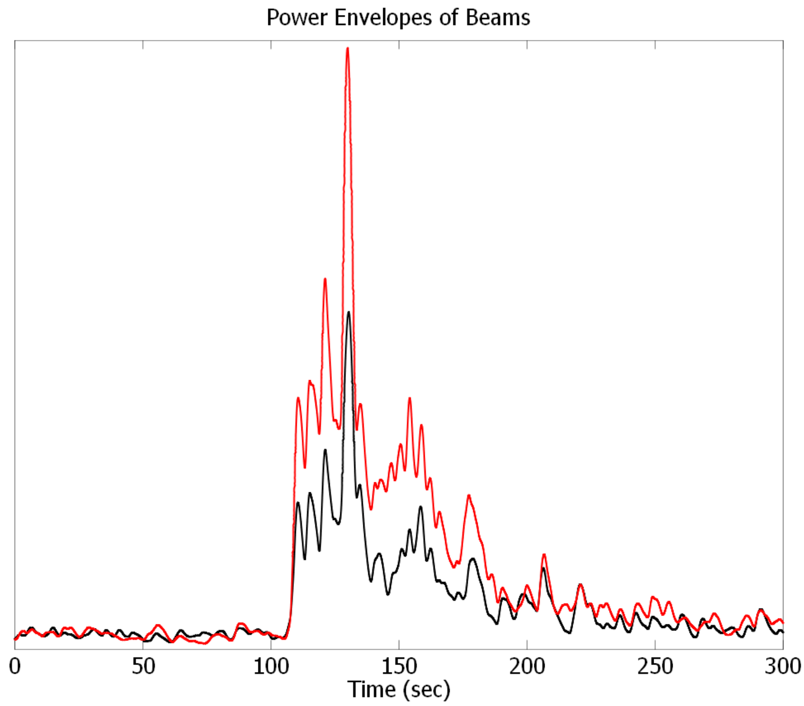

Figure 28 Approximate power envelopes for the vertical-component beam (black) and the three-component beam (red). The power signal to noise ratio of the three-component beam is about twice that of the vertical-only beam.

6. Discussion

6.1 Back-Azimuth and Slowness Estimation

A major part of regional earthquake monitoring with arrays is phase identification and association with FK analysis. Arrays contribute to phase identification by measuring the speed of wave propagation, or, equivalently, slowness, the reciprocal of speed. Phase slowness is most commonly obtained by measuring the distance of the FK peak from the origin in slowness space. Teleseismic P typically has speeds in excess of 8 kilometers per second (slownesses less than 0.125 seconds per kilometer). This characteristic separates it from regional phases, which exhibit lower speeds (higher slownesses). Typical speeds (slownesses) for the regional phases are in the range of 7-8 kilometers per second (0.12-0.15 sec/km) for Pn, 5.5-6.5 km/sec (0.15-0.18 sec/km) for Pg, 4-5 km/sec (0.2 – 0.25 sec/km) for Sn and 3-4 km/sec (0.25-0.33 sec/km) for Lg. There can be significant scatter in these values due to noise conditions at the array and variations in velocity structure beneath the array.

Phases are associated to a common event by noting their proper progression in time (Pn, then Pg, Sn, and Lg for regional phases) and by assuring that they are propagating from the same direction. This latter condition is assured by measuring similar backazimuths with an array.

We carried out a study of slowness and backazimuth measurement with the Ar Rayn array using observations of the regional and near-teleseismic earthquakes shown in Figure 29. The slowness measurements are summarized in Figure 30 as a set of histograms for phases identified as teleseismic P and the four regional phases by our analyst, Flori Ryall.

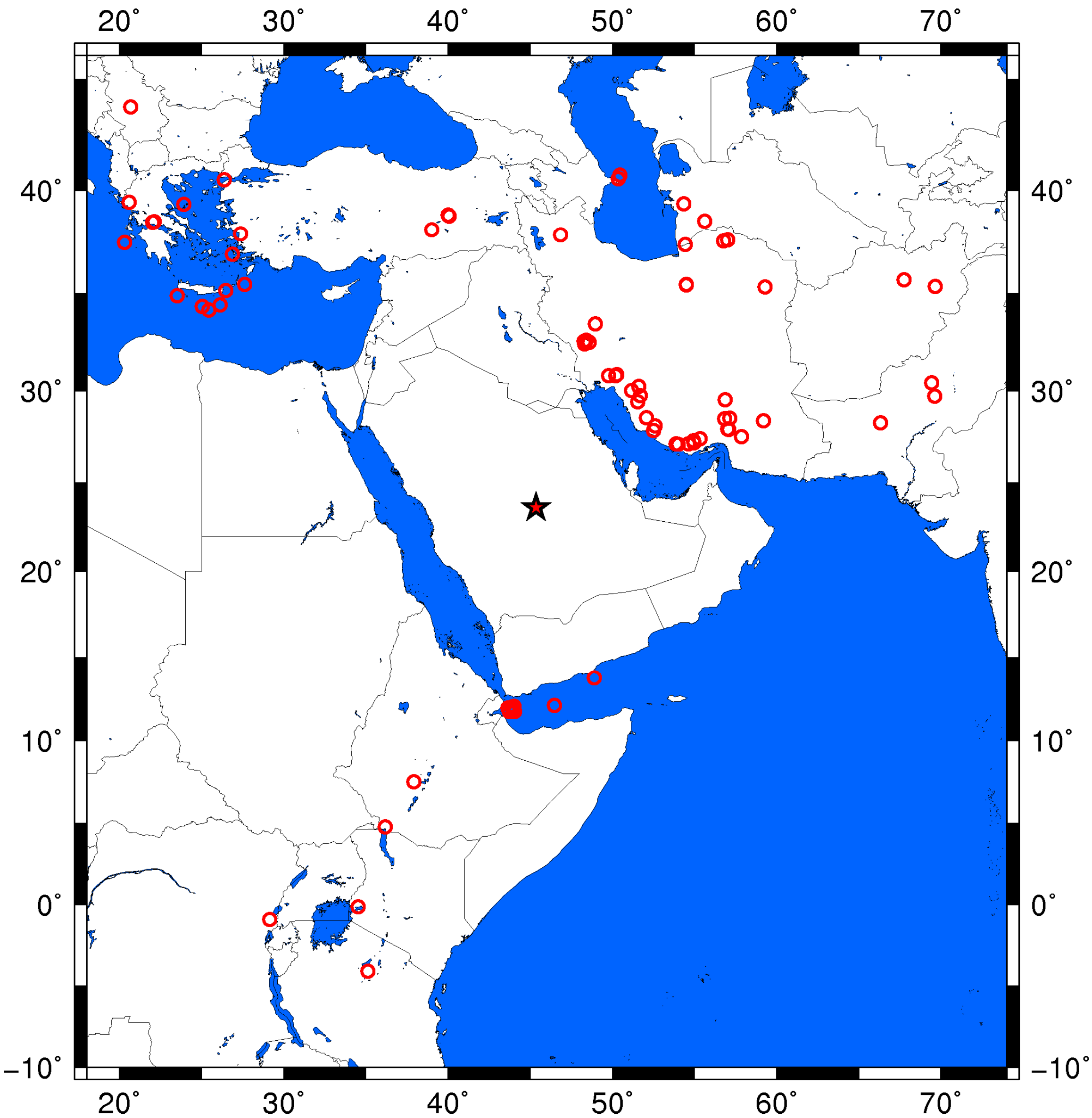

Figure 29 Distribution of events used in back-azimuth and slowness study. The array location is denoted by a star. Earthquake locations are denoted by open circles.

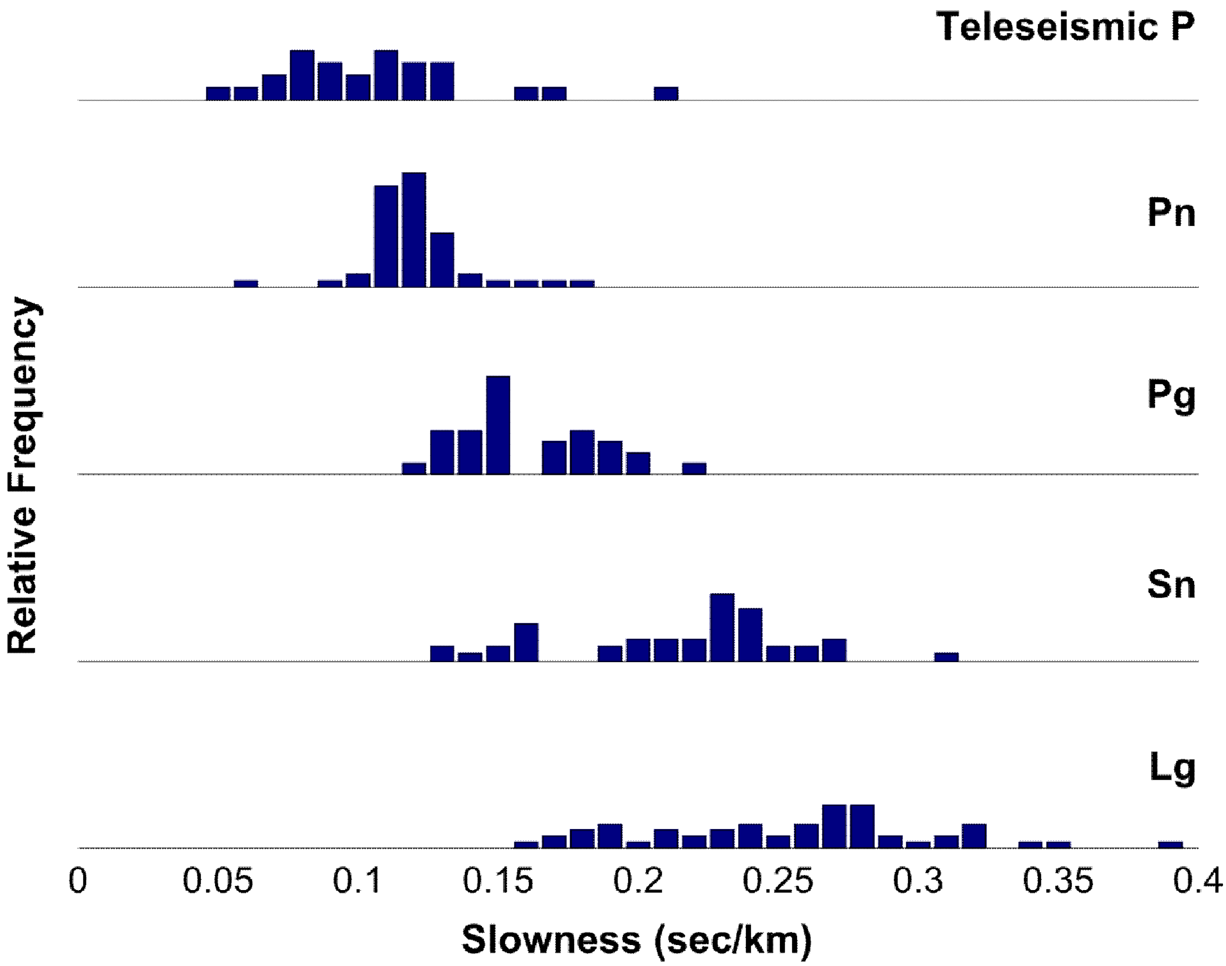

Figure 30 Slowness histograms for teleseismic P and the four regional phases Pn, Pg, Sn, and Lg. Note the increasing slowness values, but significant overlap among the phases.

The distributions of phase slowness show the anticipated progression from fast to slow values for these phases. There is quite a lot of scatter in the values, which is typical for a small-aperture array, especially in circumstances where one or more of the array elements may have been out of operation at any given time. Large slowness errors may occur due to the sidelobe structure in the array response, which is difficult to control in arrays with a modest number of sensors (less than 15-20). Slowness measurements of teleseismic waves are inaccurate with small-aperture arrays given the limited resolution (the array response has a very broad main lobe). In addition, variations in structure beneath the array (e.g. a dipping Moho) can strongly affect the apparent phase velocity for waves that approach the array from different directions. Scattering from velocity heterogeneities in the crust also can produce this effect by suppressing the coherence of seismic waves. The shear phases (Lg in particular) are most strongly affected by scattering in propagation. The later three regional phases also are superimposed on the coda of preceding waves, which can bias some measurements to lower values.

Figures 31-34 show azimuth errors for the array as a function of direction and distance from the array. In these figures, the locations of the events are indicated by points and the azimuth errors by line segments perpendicular to the direction to the array. The distance of the event from the array is indicated by the radius of the point position from the center of the plot. The true azimuth is denoted by the angle of the point position with respect to the plot center (indicated by the blue cross). The lengths of the segments are proportional to the azimuth errors and the sign of the error is indicated by the direction of the segment (negative errors are counterclockwise; positive, clockwise).

Figure 31 summarizes teleseismic P and Pn observations. There is some structure apparent in the field of azimuth errors. Events to the northwest (from the Greek archipelago, Turkey and the Greek mainland) either exhibit very little bias or counterclockwise bias. Events to the northeast (around the Caspian) exhibit small clockwise bias. Closer events at the same true azimuth (the Zagros) exhibit counterclockwise bias. Events in Africa exhibit larger counterclockwise bias. These locally consistent effects strongly suggest refraction through somewhat complicated structure beneath the array. To a degree, they also may be due to variations in structure along the paths from the events to the array. However, we note that initial P azimuth errors are modest, typically smaller than 10 degrees, consistent with experience with small-aperture arrays in other parts of the world.

Figure 32 shows the azimuth errors for teleseismic S (2 measurements only) and Sn phases. There is a consistent pattern for events in the Zagros. For S in this region, azimuth bias is opposite to the P bias, and small. Figure 33 shows Pg azimuth errors, which for Zagros events are consistent with Pn (counterclockwise).

Figure 34 summarizes Lg azimuth errors, which are considerably larger than the other phases and show no clear patterns, consistent with poor coherence of this phase across the array aperture.

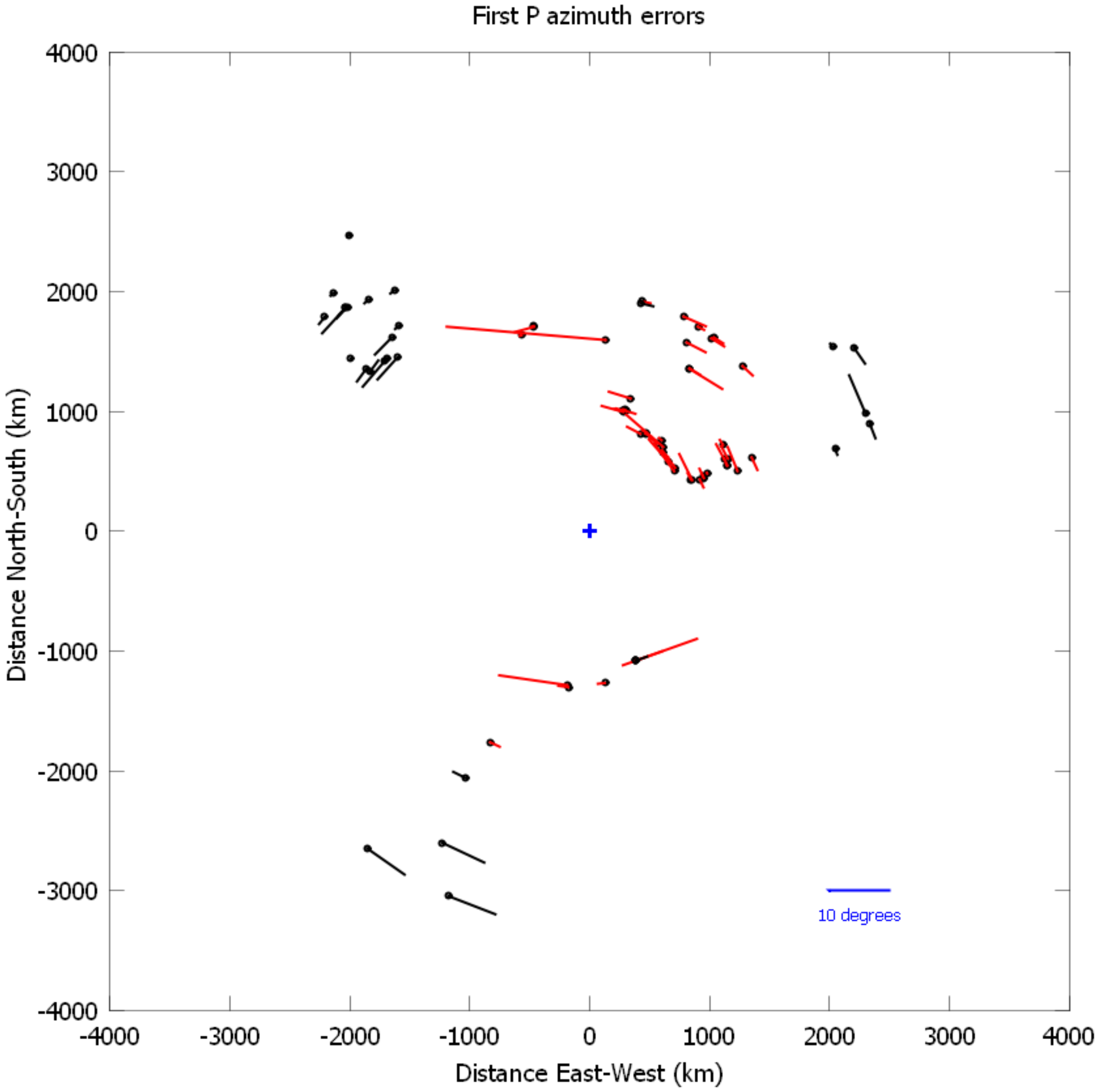

Figure 31 Spatial distribution of first P azimuth error determined from FK analysis. The location of the array is at the origin (blue cross). The points indicate event locations and the lengths of the line segments emanating from the points indicate the size of the azimuth error. Counterclockwise pointing lines indicate negative azimuth error and clockwise pointing lines indicate positive error. Pn measurements are indicated in red and teleseismic P in black. Most errors are below 10 degrees.

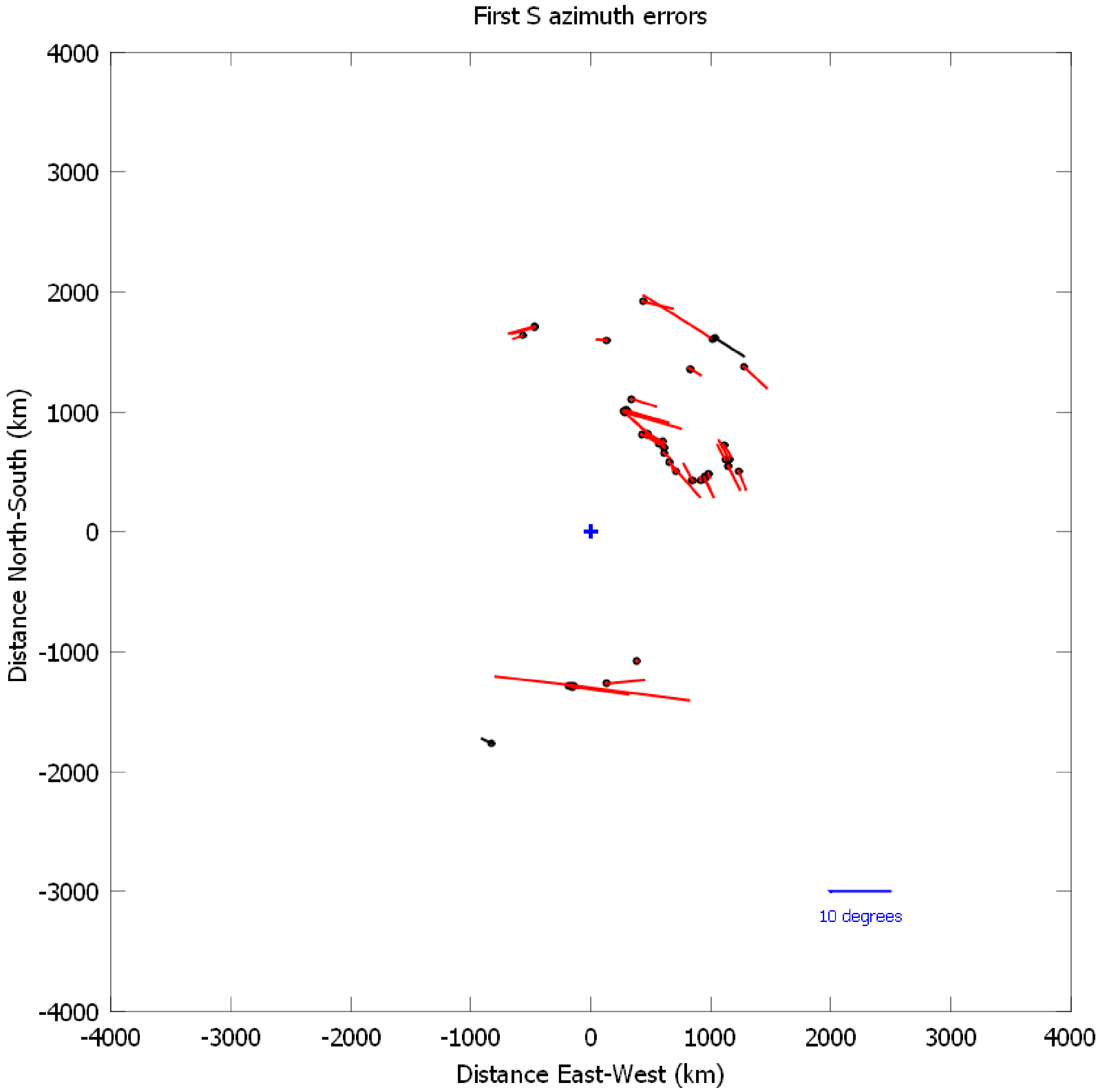

Figure 32 Spatial distribution of first S azimuth error determined from FK analysis. Sn measurements are indicated in red and teleseismic S in black.

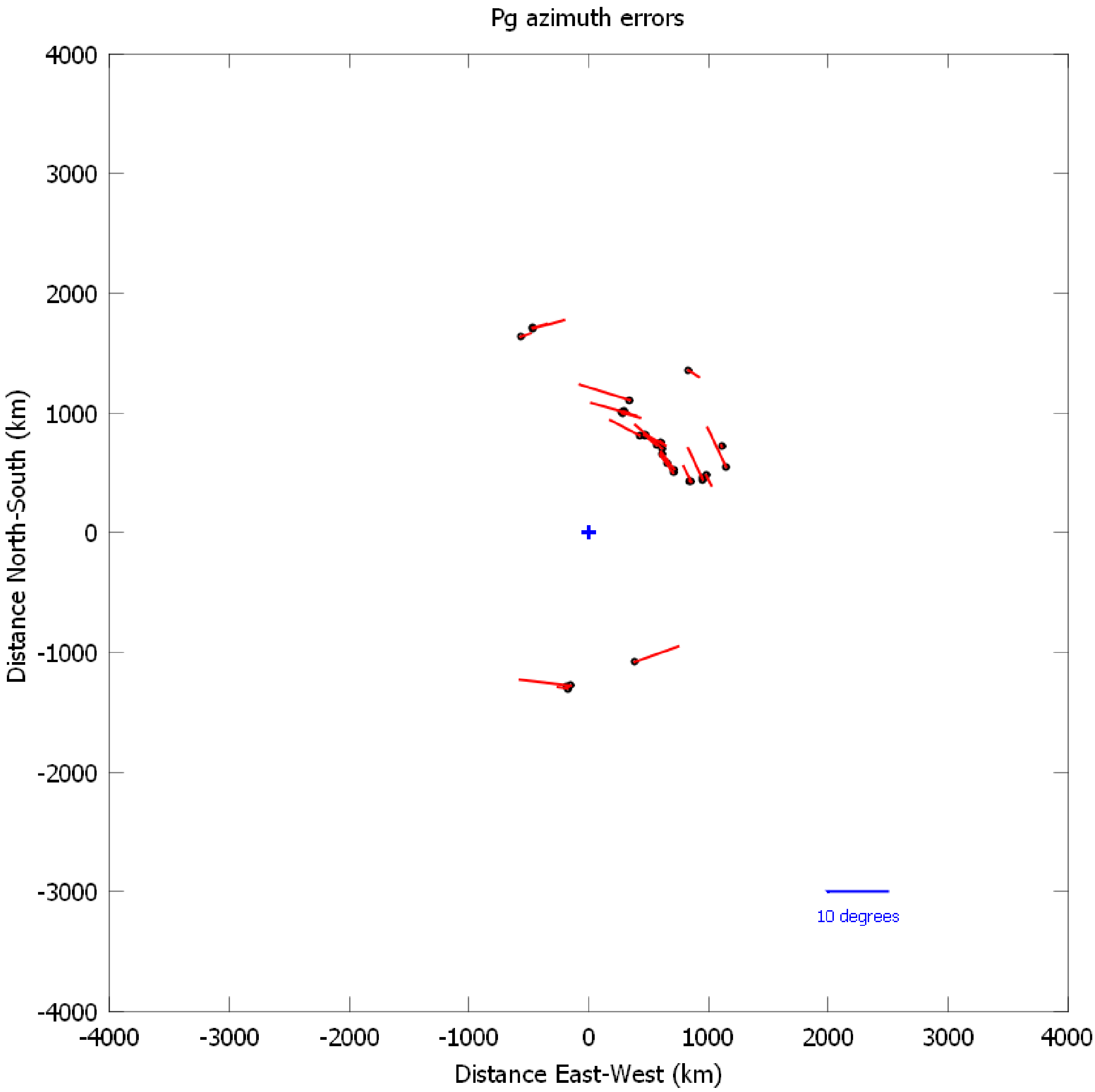

Figure 33 Spatial distribution of Pg azimuth error determined from FK analysis.

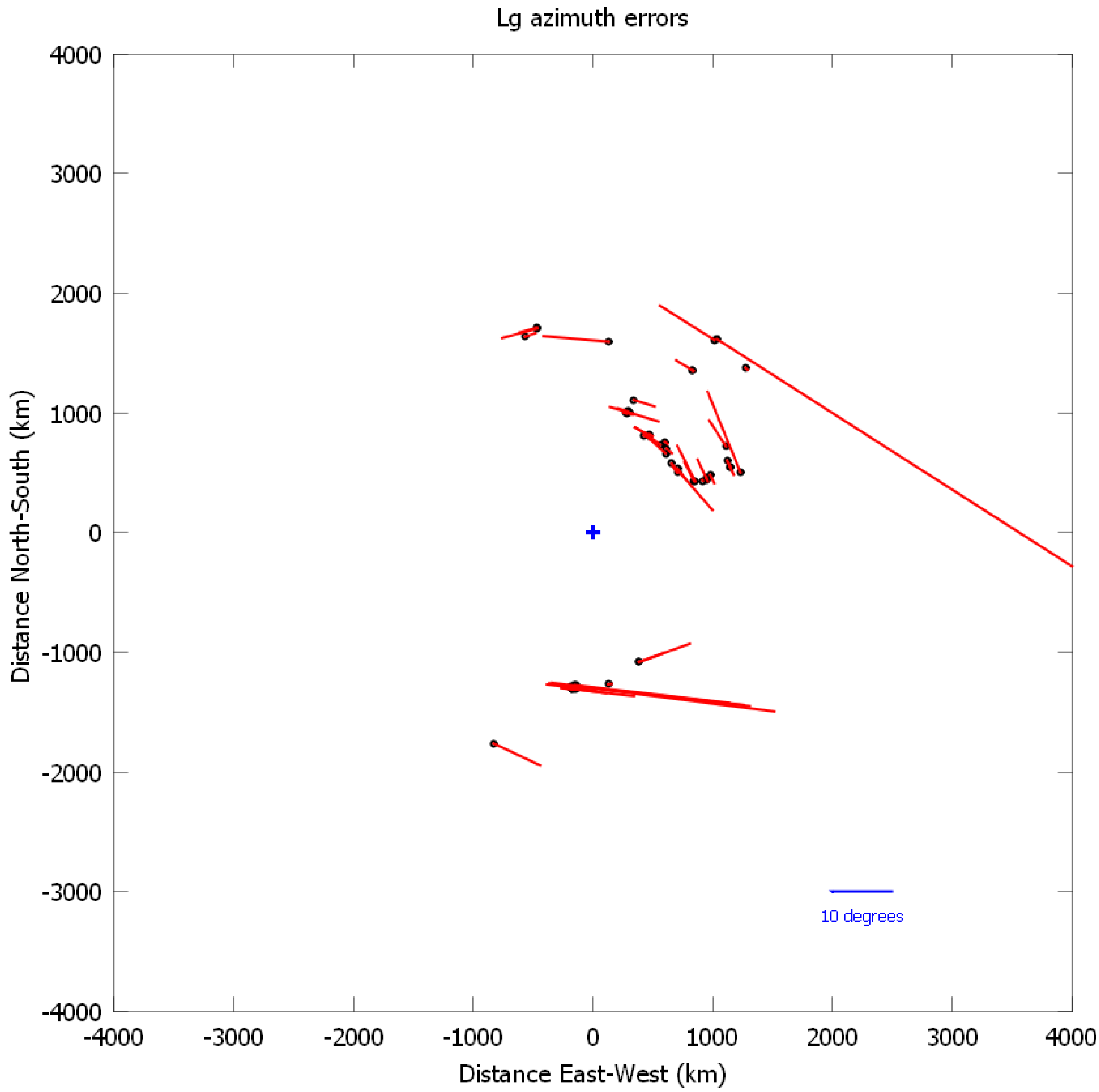

Figure 34 Spatial distribution of Lg azimuth error determined from FK analysis.

6.2 Suppression of Clutter

Earthquake swarms and aftershock sequences complicate efforts of network operators to find local and other events that may be of greater interest by producing hundreds or thousands of events that make it difficult to detect and identify other events in the region. However, an array can be used to suppress the "clutter" that these swarm events represent.

An example of this problem is illustrated with a swarm that occurred in the Gulf of Aden (map, Figure 35). The swarm began on 14 November 2010 around 06:28 GMT and was located approximately at 12 degrees north, 44 degrees east. It lasted for several weeks and comprised hundreds of events above magnitude 4. The path from the swarm to the Ar Rayn array is shown in red. Figure 36 shows 3 hours 20 minutes of data from five of the array elements at the onset of the swarm. Tens of events above magnitude four and two events above magnitude 5 occurred during this time period. It is difficult to see anything else among the swarm signals.

The map also shows the location of an earthquake (26.40N 57.22E, 14 Nov 2010 14:49:27.43 GMT) in the southern Zagros region of Iran and the path from it to the array (green). This event was of comparable size (NEIC mb 4.5) and at a similar distance from the array. Figure 37, top trace, shows 33 minutes, 20 seconds of data from a single channel of the array that contains the Zagros event. Note that its signal is weaker than the four other swarm events in this time interval.

The array can be steered to suppress the swarm events making it easier to find other events, such as the Zagros earthquake. The middle trace shows a beam using just the vertical sensors of the array. The beam has been steered to the direction and velocity of the P wave from the Zagros event. In the beam, signals from the swarm events are reduced in amplitude by a factor of 2 to 3. The signals from the Zagros event have been reduced somewhat as well owing to imperfect signal coherence across the array. It is not clear that much has been gained from this operation in making the Zagros event more visible against the background of swarm events.

However, the bottom trace is the result of applying an adaptive beamforming (equations 15 and 22) algorithm to the array outputs using both the vertical sensors of the array and the horizontal sensors. In this case, the signals from the swarm events have been reduced even further and the P wave from the Zagros event has been preserved at something like its original amplitude. This operation makes it easier to observe the Zagros event against the backdrop of swarm events. The suppression of swarm events was not complete, in part because only a portion of the array (13 of 21 channels) was in operation at the time.

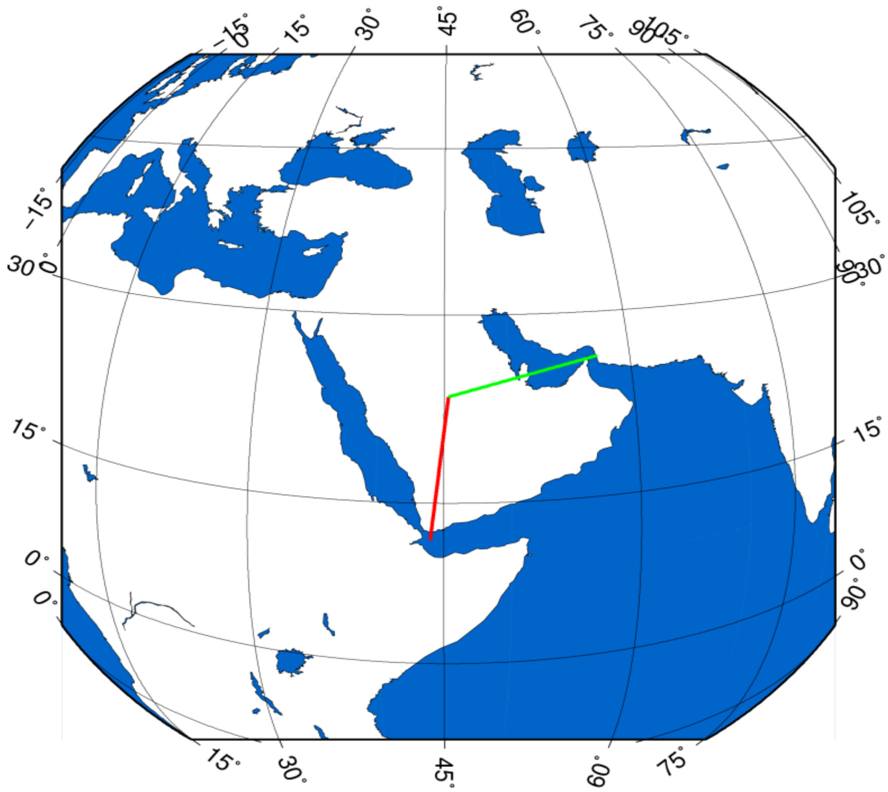

Figure 35 Location of the Gulf of Aden swarm and the single event in the southern Zagros mountains.

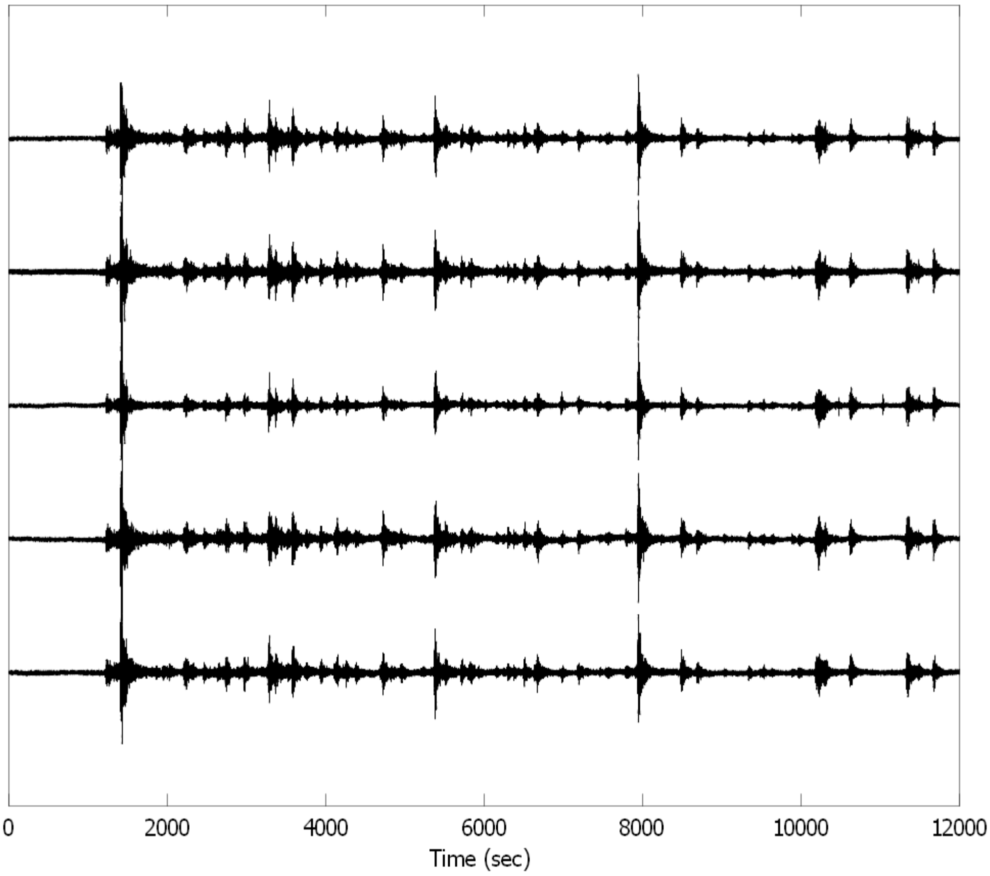

Figure 36 Adaptive beamforming example – attempt to extract a Makran event in the midst of a Gulf of Aden swarm.

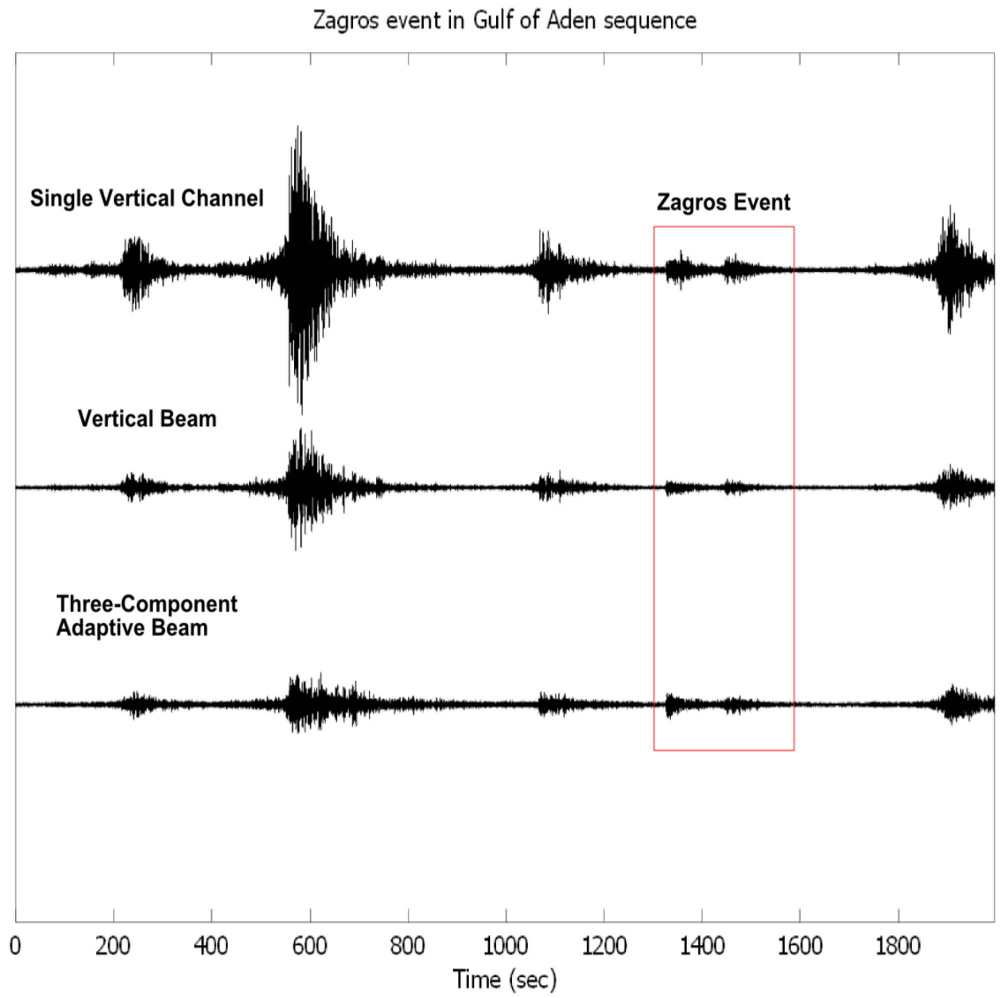

Figure 37 Adaptive beamforming effectively suppresses the Gulf of Aden signals while passing the southern Zagros P wave.

Summary & Conclusions

- The array was deployed in late 2009 using high-quality vaults and instrumentation to study seismicity and earth structure in the Arabian peninsula and surrounding regions.
- A large archive of continuous waveform data has been assembled which will provide researchers with the ability to study seismicity and structure and should be a teaching opportunity for students and staff to learn seismology and array signal processing.
- The array of three-component stations (one of a very few) allows comparison of many processing strategies.
- Based on the background noise level observed at the Ar Rayn site and the quality of seismograms from events in the region, this array could prove to be a very valuable supplement to the international Monitoring System.
- The noise level at the Ar Rayn site approaches the Peterson low noise model in the central frequency band 0.2 – 5.0 Hz.
- The most obvious discrepancy between the noise levels at the central element of the array and the Low Noise Model is in the horizontal long periods. Horizontal components are significantly noisier than the vertical component at frequencies below 0.1 Hz. At frequencies greater than 0.1 Hz, vertical and horizontal noise levels are similar. The source of the long-period noise is not clear and may be due to small tilts which affect the horizontal components more than the verticals.
- Proper installation of the array has been validated with coherence and polarization checks performed on teleseismic P phases. Coherence at 1-3 Hz is quite good for regional and teleseismic P, less good for S. This observation suggests that it would be possible to add a larger third ring to the array to enhance resolution of regional P phases and markedly improve teleseismic P processing. This capability should improve our ability to image structure of the lithosphere beneath the array.

- Standard beamforming and three-component beamforming have been performed and demonstrate the marked superiority of arrays for examine low-magnitude seismicity in the region.
- Three-component beamforming may perform better with local events, due to larger P projections onto the horizontal array elements.
- Conventional and adaptive beamforming give the analyst an ability to suppress swarm events and aftershocks, allowing studies of higher-priority local seismicity during such events.
- An initial study of backazimuth and slowness estimation with FK processing indicates good slowness measurement capability for Pn, but relatively poor capabilities for the other regional phases and teleseismic P. A third ring would substantially improve this performance.
- Backazimuth measurements for teleseismic P, Pn, Pg and Sn phases have error levels consistent with other regional arrays around the world, which would aid event formation and event location for small regional and local events not reported in catalogs.

Future work : In order to fully understand the detail seismological and seismic hazard picture of the Arabian Peninsula, this study recommends an extensive research covering :

1. This study indicates good slowness measurement capability for Pn, but relatively poor capabilities for the other regional phases and teleseismic P. Therefore, A third seismic array ring would substantially improve this performance.
2. Installation of strong motion accelerographs in various areas of the Arabian Shield is of great importance to precisely estimate the attenuation characteristics of the region and to improve seismic hazard parameters.

REFERENCES

Al-Amri, A.M. (1998). The crustal structure of the western Arabian Platform from the spectral analysis of long-period P-wave amplitude ratios, Tectonophysics, **290**, 271-283.

Al-Amri, A.M. (1999). The crustal and upper-mantle structure of the interior Arabian platform, Geophysical Journal International, **136**,421-430.

Al-Amri, A. L., R. Mellors, and F. L. Vernon (1999). Broadband Seismic Noise Characteristics of the Arabian Shield, Arabian Journal of Science and Engineering, King Fahd University of Petroleum and Minerals, 24, 99-113.

Al-Damegh, K., E. Sandvol, and M. Barazangi (2005). Crustal structure of the Arabian Plate: new constraints from the analysis of teleseismic receiver functions, *Earth Planet. Sci. Letts.*, **231**, 177-196.

Al-Damegh, K., Sandvol, E., Al-Lazki, A. and Barazangi, M. (2004). Regional wave propagation (Sn and Lg) and Pn attenuation in the Arabian plate and surrounding regions, *Geophys. J. Int.*, **157**, 775-795.

Al-Husseini M I (2000) Origin of the Arabian plate structures: Amar collision and Najd rift, GeoArabia, 5(4), 527-542

Astiz, L (1997). How to Estimate Power Spectral Density of Seismic Noise for FDSN Broadband Digital Stations", *USGS Open-File Report* 93-322, 95 pp.

Badri, M. (1991). Crustal structure of central Saudi Arabia determined from seismic refraction profiling, *Tectonophysics*, **185**, 357-374.

Benoit, M., A. Nyblade, J. VanDecar, H. Gurrola (2003). Upper mantle P wave velocity structure and transition zone thickness beneath the Arabian Shield, *Geophys. Res. Lett*. 30, 1-4.

Capon, J., J. Greenfield and R. J. Kohler, (1967). Multidimensinal maximum-likelihood processing of a large seismic array, *Proc. IEEE*, 55, 192-211.

Debayle, E., J. Leveque, M. Cara, Seismic evidence for a deeply rooted low-velocity anomaly in the upper mantle beneath the northeastern Afro/Arabian continent (2001). *Earth Planet. Sci. Lett*. 193, 423-436.

Douglas, A., (2003). Seismometer Arrays – their use in earthquake and test ban seismology, *International Handbook of Earthquake and Engineering Seismology, Part A,* 357-367.

Followill F. Harris D. B. (1983). Comments on Small Aperture Array Designs. Informal Report, Lawrence Livermore National Laboratory.

Gettings, M., H. Blank, W. Mooney and J. Healey (1986). Crustal structure of southwestern Saudi Arabia*, J. Geophys. Res.,* 91, 6491- 6512.

Johnson, D. H. and D. E. Dudgeon (1993) Array signal processing: concepts and techniques, Prentice Hall, ISBN 0130485136.

Kobayashi, H. (1970), Iterative synthesis methods for a seismic array processor, IEEE Trans. On Geoscience Electronics, **GE-8** (3), 169-178.

Looseveld R J H, Bell A, Terken J J M (1996) The tectonic evolution of interior Oman, GeoArabia, 1 (1), 28-51

Mellors, R., Preliminary noise survey and data report of Saudi Arabian data (1997). Lawrence Livermore National Laboratory internal report, August 2, 1997, UCRL-ID-128949, Office of Scientific and Technical Information, P.O. Box 62, Oak Ridge TN, 37831.

Mellors, R., Vernon, F., Camp, V., Al-Amri, A.M and Gharib, A. (1999). Regional waveform propagation in the Saudi Arabian Peninsula and evidence for a hot upper mantle under western Arabia. *J. Geophys. Res*., 104, 20,221–20,235

Moktar, T. A., C. J. Ammon, R. B. Herrmann and H. A. A. Ghalib (2001) Surface wave velocities across Arabia. *Pure. Appl. Geophys*., 158, 1425-1444.

Mooney, M. Gettings, H. Blank, J. Healy, Saudi Arabian seismic refraction profile: A traveltime interpretation of crustal and upper mantle structure (1985). *Tectonophysics* 111, 173-246.

Mykkeltveit S. Åstebøl K. Doornbos D. J. Husebye E. S. (1983). Seismic array configuration optimization, *Bull. Seism. Soc. Am*. 73, 173-186.

Mykkeltveit S. Fyen J. Ringdal F. Kværna T. (1990a). Spatial characteristics of the NORESS noise field and implications for array detection processing. *Phys. Earth Planet. Interiors*, 63, 277-283.

Mykkeltveit, S., F. Ringdal, T. Kvaerna and R. Alewine (1990b). Application of regional arrays in seismic verification, *Bull. Seism. Soc. Am*., 80, 1777-1800.

Park, Y., A. Nyblade, A. Rodgers and A. M Al-Amri (2007). Upper mantle structure beneath the Arabian Peninsula from regional body-wave tomography: Implications for the origin of Cenozoic uplift and volcanism in the Arabian Shield, *Geochemistry, Geophysics, Geosystems*, 8, doi:10.1029/2006GC001566.

Pasyanos, M., E. Matzel, W.. Walter, and A. Rodgers (2009). Broad-band Lg attenuation modeling in the Middle East, *Geophys. J. Int., 177*, 1166-1176.

Peterson., J. (1993). Observations and modeling of seismic background noise, USGS Open-File Report 93-322.

Powers R W, Ramirez L F, Redmond C D, Elberg E L (1966). Geology of the Arabian Peninsula, Sedimentary geology of Saudi Arabia: U. S. Geological Survey professional paper 560-D D1-D147

Rodgers, A., W. Walter, R. Mellors, A. M. S. Al-Amri and Y. S. Zhang (1999). Lithospheric structure of the Arabian Shield and Platform from complete regional waveform modeling and surface wave group velocities, *Geophys. J. Int*., 138, 871-878.

Rost, S., and C. Thomas (2002). Array seismology: methods and applications, *Reviews of Geophysics*, 40, 2-1-2-27.

Sandvol, E., D. Seber, M. Barazangi, F. Vernon, R. Mellors and A. Al-Amri (1998). Lithospheric discontinuities beneath the Arabian Shield, *Geophys. Res. Lett*., 25, 2873-2877.

Schweitzer, J., J. Fyen, S. Mykkeltveit and T. Kvaerna (2009), Seismic arrays, chapter 9 in Bormann, P. (Ed.). New Manual of Seismological Observatory Practice (NMSOP-1), IASPEI, GFZ German Research Centre for Geosciences, Potsdam, DOI: 10.2312/GFZ.NMSOP_r1_ch9

Tkalčiģ, H., M. Pasyanos, A. Rodgers, R. Gok and A. Al-Amri (2006). A multi-step approach for joint modeling of surface wave dispersion and teleseismic receiver functions: Implications for lithospheric structure of the Arabian Peninsula. *J. Geophys. Res*., 111, B113111, doi:10.1029/2005JB004130.

Van Trees, H. L. (2002) Detection estimation and modulation theory: Optimum array processing, Wiley-Interscience, ISBN 0471093904.

Vernon, F., and J. Berger (1997). Broadband seismic characterization of the Arabian Shield, Final Scientific Technical Report, Department of Energy Contract No. F 19628-95-K-0015, 36 pp.

PUBLICATIONS/PRESENTATIONS

1. PUBLICATIONS

As we stated in the original proposal, we plan to publish at least two papers in from the outcome of the project.

A. The first paper has been accepted already in a reputable ISI journal " Seismological Research Letters " and will appear for publication in November 2011. The paper entitled "**A Regional Seismic Array of Three-Component Stations in Central Saudi Arabia ''.**

SEISMOLOGICAL RESEARCH LETTERS Impact Factor

Journal Abbreviation: SEISMOL RES LETT

Journal ISSN: 0895-0695

Year	Impact Factor (IF)	Total Articles	Total Cites
2010	2.317	72	1303
2009	1.714	67	1099
2008	1.826	67	952

B. We are preparing the manuscript of the second paper as well for publication in ISI journal in 2012.

2. PRESENTATIONS

So far, We presented the outcome of the research project and acknowledged NPST in the following conferences.

A. American Geophysical Union, San Francisco, Dec. 12-16 , 2010

B. Arabian conference of Geosciences, Riyadh , April 28 – 30, 2011

C. To be presented Insha Allah in the '' 4th International Professional Geology Conference , Vancouver, Canada, January 22 -24, 2012.